Nonlinear Energy Transfer among Ocean Internal Waves in the Wake of a Moving Cyclone

AGOSTINO N. MERONI

Department of Earth and Environmental Sciences, University of Milan-Bicocca, Milan, Italy

MADELINE D. MILLER

Department of Earth and Planetary Sciences, Harvard University, Cambridge, Massachusetts

ELI TZIPERMAN

Department of Earth and Planetary Sciences, and School of Engineering and Applied Sciences, Harvard University, Cambridge, Massachusetts

CLAUDIA PASQUERO

Department of Earth and Environmental Sciences, University of Milan-Bicocca, Milan, Italy

(Manuscript received 18 October 2016, in final form 18 May 2017)

ABSTRACT

The nonlinear dynamics leading to the generation of superinertial internal waves in the ocean, in the wake of a cyclonic storm, is investigated by means of theoretical arguments and of numerical integration of the hydrostatic Boussinesq equations in a simplified, realistic, open-ocean setting. The velocity fields are first decomposed into internal baroclinic modes, and then the energy transfer across modes and at different frequencies is calculated analytically. The energy transfer across modes is dominated by the advection of high-mode m waves by the second- and third-mode waves ($n = 2$ or 3), which are the most energetic, and this results in the excitation of the $l = m - 2$ or $m - 3$ mode wave at the double-inertial frequency. The analyzed nonlinear interactions lead to a transfer of energy from near-inertial waves, directly excited by the storm, to superinertial waves, which typically propagate faster and farther than their lower-frequency parents and can lead to internal mixing even at large distances from the region of large air–sea momentum fluxes. Energy is found to flow from large to small scales as well. Thus, the double-inertial peak formation is thought to represent a small but fundamental intermediate step in the energy cascade toward dissipation.

1. Introduction

Internal waves are ubiquitous in the ocean and show almost universal spectral features described by the empirical spectrum developed by Garrett and Munk (1972, 1975, 1979). The physical processes responsible for the observed spectrum are still to be fully understood, but the waves are forced mostly by atmospheric forcing (Rubenstein 1994; Nilsson 1995) and tide–topography interactions (Sjöberg and Stigebrandt 1992), and the spectrum is believed to be the result of nonlinear interactions.

Internal waves are important among other reasons because they play a nonnegligible role in ocean interior mixing, which is known to be very spatially inhomogeneous (Polzin et al. 1997; Whalen et al. 2012; Waterhouse et al. 2014) but still not yet fully understood (Ledwell et al. 1993; Munk and Wunsch 1998; Ledwell et al. 2000; Heywood et al. 2002; Eden 2011, 2012; Olbers and Eden 2013; Griesel et al. 2015).

Internal waves propagate from their forcing regions into the interior of the ocean, where they can interact nonlinearly (Olbers 1976; McComas and Bretherton 1977; Ripa 1981; Müller et al. 1986) and, when they become unstable, finally break. With their breaking, they contribute to the vertical diapycnal mixing of heat, salt, and dissolved chemical species (Olbers 1974, 1976;

Corresponding author: Agostino N. Meroni, a.meroni9@campus.unimib.it

DOI: 10.1175/JPO-D-16-0232.1

Hibiya et al. 1996) and, since they transport energy and momentum, they can induce mean flow changes (Staquet and Sommeria 2002).

Among the atmospheric sources of oceanic internal waves, there are both the climatological winds and the more intermittent and nonuniformly distributed intense wind events, such as tropical cyclones. Estimates of the annual-mean, upper-ocean thermal diffusivity resulting from the passage of tropical cyclones are $O(10^{-5})$ or $O(10^{-4})\,\mathrm{m^2\,s^{-1}}$ (Korty et al. 2008; Sriver and Huber 2007), at least 10 times larger than the observed background tropical thermocline thermal diffusivity (Ledwell et al. 1998). This happens because momentum fluxes depend nonlinearly on wind intensity, and it means that, even if intermittent and localized, tropical cyclones' contribution to the upper-ocean mixing is nonnegligible.

Geisler (1970) showed in his linear analysis that if the hurricane speed is greater than the eigenspeed of the wave (in terms of the internal mode decomposition, as clarified in what follows), the baroclinic response of the ocean is excited. In a continuously stratified ocean, this means that the storm has a three-dimensional, near-inertial, internal wave wake. Instead, if the hurricane is too slow, there is no wake. Tropical cyclones usually move with a speed that ranges from 1 to $10\,\mathrm{m\,s^{-1}}$, and the eigenspeeds are typically smaller than $3\,\mathrm{m\,s^{-1}}$, which means that tropical cyclones are generally effective sources of internal waves. Geisler (1970) also showed that the pressure anomaly of the tropical cyclone induces a deformation in the free-surface height but has a very small effect on the baroclinic oscillating response. In fact, by writing the equation for the baroclinic mode he explicitly showed that the forcing due to the pressure low is negligible compared to the forcing due to the wind stress. Another linear solution to the equations of motion in the ocean forced by a moving cyclone was given by Gill (1982, chapter 9), who found a resonant behavior in the energy of the vertical velocity oscillations as a function of the translation speed of the hurricane. In particular, if the residence time of the storm (the ratio of its typical length to its translation speed) is close to the local inertial period (the inverse of the Coriolis parameter), the coupling between the forcing and the inertial currents is very efficient and the tropical cyclone can transfer energy to the ocean optimally. The sensitivity of the response to the hurricane translation speed was further studied by Greatbatch (1984), Samson et al. (2009), and Mei et al. (2012) with both numerical simulations and data analysis. A detailed theoretical description of the energy transfer from a translating hurricane to the ocean was given by Nilsson (1995).

Many other works focused on the dynamical and thermodynamical response of the ocean to hurricanes (Price 1981; Chang and Anthes 1978; Sanford et al. 2007; D'Asaro et al. 2007; Black and Dickey 2008) and their consequence on the global climate and meridional heat transport (Pasquero and Emanuel 2008; Jansen and Ferrari 2009; Jansen et al. 2010). The focus of this paper is on the generation mechanism of superinertial waves, that is, waves with a frequency equal to the double (or higher multiple) of the local Coriolis parameter. They were first found by Price (1983) in his numerical study of the internal wave wake but no explanation of their generation was given. The main interest in studying these superinertial waves is that they can propagate further than the near-inertial ones (Niwa and Hibiya 1997; Zedler 2009) and thus they can supply energy to the local internal wave field far from their generation region. In fact, the lower limit of the range of frequency of internal waves is determined by their latitude, and the upper one is determined by the local stratification. In particular, the Coriolis parameter sets the minimum value of frequency of an internal wave that can be sustained by the system. Thus, if a wave is traveling poleward and if its frequency $\omega = f_0 + \varepsilon$ is close to the Coriolis parameter f_0 at the initial latitude ϕ_0 (a near-inertial internal wave), it may reach a latitude ϕ_1 at which the Coriolis parameter f_1 equals the frequency of the wave $f_1 = f_0 + \varepsilon$. At higher latitude ($\phi_2 > \phi_1$, with $f_2 > f_1$), the wave would have a frequency that falls out of the admissible frequency range for internal waves, and thus it experiences internal reflection at the critical latitude ϕ_1 (Kroll 1975; Munk 1981; Garrett 2001), unless in presence of an appropriate mean flow (Gerkema et al. 2013; Xie et al. 2016). It is clear that superinertial waves are less prone to critical latitude reflection and can therefore propagate farther than near-inertial ones.

Niwa and Hibiya (1997) analyzed the superinertial wave field using an internal baroclinic mode decomposition of a uniformly stratified ocean. With such analysis, low modenumbers correspond to large vertical scales, and high modenumbers correspond to small vertical scales. They discovered that the most prominent superinertial waves appear in the lowest mode, and in particular they studied with a bispectral analysis the high-mode, near-inertial waves that interact to give the first-mode, double-inertial waves. They found that some couples of modes contribute to the formation of the first-mode, double-inertial waves, while others subtract energy from them. Thus, the energy flows in both directions, and this might suggest that the formation of the double-inertial peak plays a role in the energy cascade toward the small scales. The limit of their explanation is that the stratification is uniform, which means that a realistic oceanic vertical structure (mixed layer and thermocline) is not included. Their analysis is simplified

because the baroclinic modes of a uniformly stratified ocean are sinusoidal functions, and therefore the mode-enumber is directly proportional to the vertical wavenumber. The case of nonuniform stratification is much harder to treat with the bispectral approach because there is no direct relation between a vertical wavenumber and an internal baroclinic mode.

Danioux and Klein (2008) generalized Niwa and Hibiya's (1997) results to a nonuniform stratification profile using a perturbation approach. They considered a zonal barotropic jet $U = U(y)$ and showed that a necessary condition for nonlinear interactions that generate waves at $2f$ is that the relative vorticity of the mean flow $\zeta = -dU/dy$ has a nonzero Fourier component at the wavenumber that corresponds to the double-inertial wave $\mathbf{k}_{2f}$. They showed that the generation mechanism is local in wavenumber space and is driven by the eddy relative vorticity field acting at the right wavenumber $\mathbf{k}_{2f}$ through a resonant mechanism due to the advective terms. They also proved that a single internal mode can interact with itself and generate super-inertial motion.

Zedler (2009) used a numerical study over an ocean region with a realistic initial density profile, showing that the nonlinear interactions take place in the region of the mixed layer and the upper thermocline (first 200 m in her setup) and then are radiated to the interior through vorticity conservation as a linear mode. This seems to be in conflict with Niwa and Hibiya's (1997) result, which states that nonlinear interactions take place throughout the entire water column. But since a thorough description of the vertical structure of the stratification down to the bottom of the ocean was not included in the work, it is hard to explain whether the differences with respect to Niwa and Hibiya's (1997) results are an effect of the different stratification. This would be the interpretation in a WKB scaling, in which the energy scales with the stratification (Gill 1982). In fact, the energy exchanges would dominate the region of maximum $N = N(z)$, the buoyancy frequency, which is the upper ocean in the case of Zedler (2009) and the entire water column in the case of Niwa and Hibiya (1997).

In this paper, Niwa and Hibiya's (1997) normal-mode analysis is extended to a nonuniformly stratified ocean to give a detailed and quantitative description of the exchange of energy between the waves excited by the tropical cyclone. The nonlinear hydrostatic Boussinesq equations are solved with two numerical simulations, and an analytical theory is developed to describe the nonlinear interactions of the linear solutions, with a slightly simplified set of equations. In particular, a set of coefficients that measure the energy transfers between modes is derived analytically.

In section 2, the numerical model and the equations of motion used in the theoretical analysis are introduced. Section 3 describes how to decompose the nonlinear equations on the normal modes, and in section 4, the analytical theory that introduces the energy transfer coefficients in the spectral domain is developed. Sections 5 and 6 are devoted to the presentation of the results and the conclusions.

2. Numerical model and equations of motion

The problem is studied by solving numerically the fully nonlinear set of hydrostatic Boussinesq primitive equations on an f plane. This is accomplished with two simulations run with the Regional Ocean Modeling System–Adaptive Grid Refinement in Fortran (ROMS_AGRIF) in a simplified realistic setup. ROMS is a three-dimensional, free-surface, split-explicit ocean model (Penven et al. 2006; Debreu et al. 2012).

The main difference between the two simulations is the horizontal extent of the domain. In the simulation called D4000, the flat basin is 4000 km × 4000 km wide with a horizontal resolution of 20 km, while in the simulation D8000, the sides of the square basin are 8000 km and the horizontal resolution is 40 km. The numerical ocean is 5 km deep ($H = 5000$ m), and is discretized on a grid with 44 vertical levels, with different thicknesses, ranging from 7 m at the top to 500 m at the bottom. Turbulent vertical mixing is accomplished via the nonlocal K-profile parameterization (KPP; Large et al. 1994), the horizontal diffusion is set to zero, and open boundary conditions on all sides allow the waves to propagate outside of the basin, significantly reducing their reflection.

The initial conditions are set analytically. The initial velocity field and the initial free-surface height are zero everywhere. The potential temperature vertical profile, independent of the horizontal position, is chosen to have a climatological mixed layer depth $H_{\mathrm{mix}} = 50$ m and then an exponential decaying profile, with a length scale $\lambda = 400$ m, namely,

$$\theta(z) = \begin{cases} \theta_s & \text{for} \quad -H_{\mathrm{mix}} < z \le 0 \\ \theta_d + \Delta\theta e^{(H_{\mathrm{mix}}+z)/\lambda} & \text{for} \quad -H < z < -H_{\mathrm{mix}} \end{cases}, \tag{1}$$

where $\theta_s = 22$°C is the surface temperature, $\theta_d = 2$°C is the temperature at depth, and $\Delta\theta = \theta_s - \theta_d$. The salinity has a constant value everywhere equal to 35 psu, so that variations in density come directly from variations in temperature through the nonlinear equation of state implemented in the model [with the split equation of state (SPLIT_EOS) option activated]. This equation is described by Shchepetkin and McWilliams (2003) and

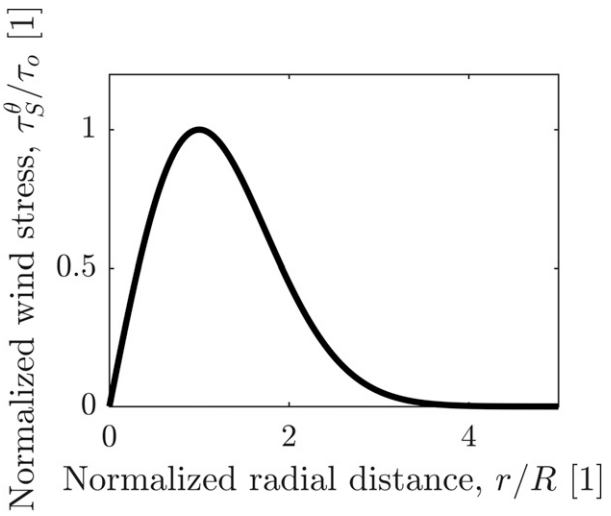

FIG. 1. Radial profile of the wind stress considered, as defined in Eq. (2).

is a modified version of the one described by Jackett and McDougall (1995).

Momentum, temperature, and salinity fluxes are defined as top and bottom boundary conditions. In the simulations, the bottom stress, the freshwater flux, and the heat flux are zero. No pressure low associated with the tropical cyclone is considered because Geisler (1970) showed that it does not influence the internal wave wake, which is the object of this study. The only nonzero forcing is the surface wind stress, which is modeled as a radially symmetric vortex. In a reference frame moving with the storm, the wind stress is only tangential, it increases linearly with the distance for small radii, and then has a Gaussian-like decay (Nilsson 1995). In polar coordinates $\{r, \theta\}$ such a vortex with the center in the origin of the reference frame is defined as

$$\tau_s^r = 0, \quad \tau_s^\theta = \tau_o (r/R) \mathrm{e}^{(1-r^2/R^2)/2}, \tag{2}$$

where the constant τ_o is the maximum value of the wind stress, attained at the distance R from the center (see Fig. 1). The values are chosen to be $R = 200\,\mathrm{km}$ and $\tau_o = 1\,\mathrm{Pa}$. In a short, initial phase, starting when the vortex center is still out of the domain, the amplitude of the wind stress increases from zero to the maximum value $\tau_o = 1\,\mathrm{Pa}$. Then, it moves at constant speed $U = 5\,\mathrm{m\,s^{-1}}$ from east to west on a horizontal line in the middle of the basin, which is itself centered at 15° latitude north on an f plane, where the inertial frequency is $f/2\pi \simeq 6 \times 10^{-5}\,\mathrm{s^{-1}}$, which corresponds to a period of roughly 46 h. The duration of the simulations is chosen so that they begin when the storm center is one diameter (400 km) out of the eastern edge of the domain, and they end when the storm center is one diameter out of the western edge.

With respect to the set of equations integrated by the numerical model, a slightly simplified set is introduced here to develop the analytical theory. First, it is assumed that the equation of state is linear. This means that since salinity is uniform and constant, the adiabatic equation for density can replace the temperature equation. Then, vertical diffusivity is set to zero, and the wind stress, instead of imposing the momentum flux at the surface, acts as a body force over the entire mixed layer depth. Thus, the analytical theory is built on the following equations:

$$\frac{\partial u}{\partial t} + \left(u\frac{\partial}{\partial x} + v\frac{\partial}{\partial y} + w\frac{\partial}{\partial z}\right)u - fv = -\frac{1}{\rho_o}\frac{\partial p}{\partial x} + \frac{1}{\rho_o}\frac{\tau_s^x}{H_{\mathrm{mix}}}\sigma(z), \tag{3}$$

$$\frac{\partial v}{\partial t} + \left(u\frac{\partial}{\partial x} + v\frac{\partial}{\partial y} + w\frac{\partial}{\partial z}\right)v - fu = -\frac{1}{\rho_o}\frac{\partial p}{\partial y} + \frac{1}{\rho_o}\frac{\tau_s^y}{H_{\mathrm{mix}}}\sigma(z), \tag{4}$$

$$\frac{\partial p}{\partial z} + \rho g = 0, \tag{5}$$

$$\frac{\partial u}{\partial x} + \frac{\partial v}{\partial y} + \frac{\partial w}{\partial z} = 0, \quad \text{and} \tag{6}$$

$$\frac{g}{\rho_o}\left[\frac{\partial \rho}{\partial t} + \left(u\frac{\partial}{\partial x} + v\frac{\partial}{\partial y} + w\frac{\partial}{\partial z}\right)\rho\right] - wN^2 = 0. \tag{7}$$

The usual symbols are used: f is the Coriolis parameter; u, v, and w are the velocity components; τ_s^x and τ_s^y are the Cartesian components of the surface wind stress; and ρ and p are the density and the pressure anomalies with respect to the reference profiles $\rho_o + \hat{\rho}(z)$ and $\hat{p}(z)$, which are in hydrostatic balance and with $|\rho|, |\hat{\rho}| \ll \rho_o$ and $|p| \ll \hat{p}$. The profile $\rho_o + \hat{\rho}(z)$ is defined so that its vertical derivative is equal to the adiabatic vertical derivative of the total density in its unperturbed state. This means that the density anomaly ρ plays the role of a locally referenced potential density, and it is suitable for calculating the squared buoyancy frequency profile:

$$N^2 = -\frac{g}{\rho_o}\frac{\partial \rho}{\partial z}, \tag{8}$$

where g is the acceleration due to gravity (Shchepetkin and McWilliams 2003). The depth of the mixed layer is denoted with H_{mix}, and the step function is $\sigma(z) = 1$ if $-H_{\mathrm{mix}} < z < 0$ and $\sigma(z) = 0$ otherwise.

At the flat bottom $z = -H$, the boundary condition is $w = 0$, and, since the baroclinic modes are found in the rigid-lid approximation (Gill 1982), at the surface $z = 0$, the condition $w = 0$ holds as well.

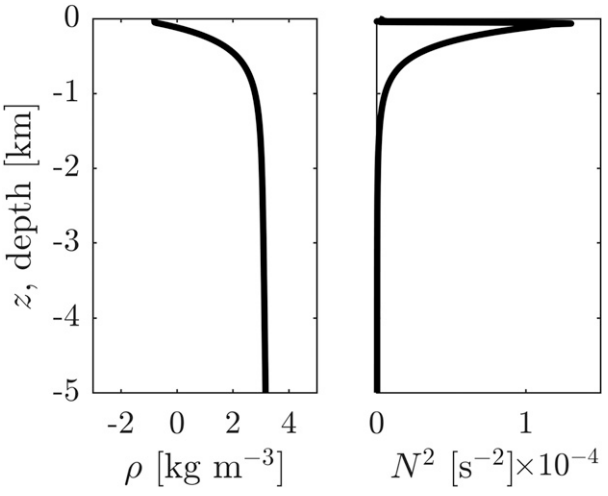

FIG. 2. (left) The unperturbed density anomaly vertical profile ρ and (right) the squared buoyancy frequency N^2, as defined in Eq. (8).

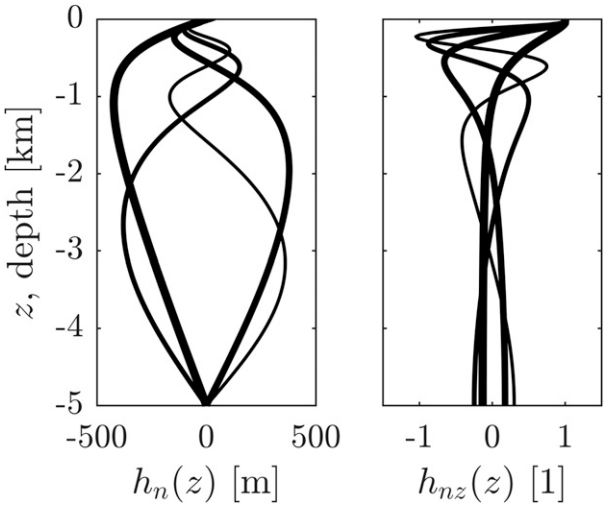

FIG. 3. First four baroclinic modes $h_n(z)$ and their vertical derivatives $h_{nz}(z)$ for $n = 1, \ldots, 4$. The thickness of the lines decreases with increasing modenumber.

3. Internal mode decomposition

The internal modes have largely proved to be a valuable tool to describe the vertical structure of the response of the ocean to wind forcing (Pollard 1970; Gill 1982, 1984; Kundu and Thomson 1985; Shay et al. 1989; Nilsson 1995). In this section, the nonlinear equations, Eqs. (3)–(7), are projected on the internal modes.

Following the notation used by Nilsson (1995), the internal baroclinic modes $h_n(z)$ and the correspondent eigenspeed c_n, with $n \in \mathbb{N}, n \geq 1$, are the solutions of the Sturm–Liouville problem

$$\frac{h_{nzz}}{N^2} + \frac{h_n}{c_n^2} = 0 \quad \text{with} \quad h_n(0) = h_n(-H) = 0, \tag{9}$$

where the subscript z denotes derivation with respect to the vertical direction, and N is the buoyancy frequency profile considered.

Since the normal modes are defined up to a multiplicative constant, a normalization condition has to be imposed, and a common choice is $h_{nz}(0) = 1$. The buoyancy frequency corresponding to the unperturbed anomaly density profile obtained from the numerical simulations (both shown in Fig. 2) is used to numerically calculate the internal baroclinic modes of the problem by solving Eq. (9). The first four modes are shown in Fig. 3 together with their vertical derivatives. The modes calculated in this way are used both in the analysis of the simulations and in the analytical part of this work.

The complete theory of normal modes includes also the barotropic one. However, at least since Geisler (1970), it is known that there is no barotropic contribution to the wave wake. Moreover, as in the present study, direct calculations show that the role of the barotropic mode is negligible; only the baroclinic modes are considered here.

The dynamical variables can be projected on the internal modes as

$$w = \sum_{l=1}^{+\infty} w_l h_l, \tag{10}$$

$$[u, v, p/\rho_o, \sigma] = \sum_{l=1}^{+\infty} [u_l, v_l, p_l, \sigma_l] h_{lz}, \quad \text{and} \tag{11}$$

$$-\rho/\rho_o = \sum_{l=1}^{+\infty} \eta_l h_{lzz}, \tag{12}$$

where h_l and their vertical derivatives h_{lz} and h_{lzz} contain all the dependence on the depth z, and the expansion coefficients are a function of (x, y, t). By exploiting the orthogonality of the internal modes (Gill 1982, chapter 6), the expansion coefficients can be found as

$$w_l = \frac{\int_{-H}^{0} dz\, N^2 h_l w}{\int_{-H}^{0} dz\, N^2 h_l^2},$$

$$[u_l, v_l, p_l, \sigma_l] = \frac{\int_{-H}^{0} dz\, h_{lz} [u, v, p/\rho_o, \sigma]}{\int_{-H}^{0} dz\, h_{lz}^2},$$

$$\eta_l = p_l / g,$$

with the last equality given by the hydrostatic equation. These integrals are calculated directly with the outputs of the simulations to find the projections of the fully nonlinear solutions.

Using the decomposition introduced above [Eqs. (10)–(12)], it is well known that the linearized governing equations for a stratified ocean can be replaced by an infinite set of linear, shallow-water equations (Gill 1982, chapter 6). In particular, η_l plays the role of the free-surface height, and with the definitions of equivalent depth $H_l = c_l^2/g$ and equivalent forcing depth $H_l^F = H_{\mathrm{mix}}/\sigma_l$, the dynamics is described by the linear, shallow-water equations in the variables u_l, v_l, and η_l. This linear problem was solved by Gill (1982, chapter 9), who showed that the energy of the waves is concentrated in a peak around the nondimensional frequency

$$\frac{\omega_{Gl}}{f} = \frac{1}{\sqrt{1 - c_l^2/U^2}}, \tag{13}$$

where c_l is the eigenspeed of the mode considered, and U is the storm translation speed. Then, Shay et al. (1989) solved the problem by finding its Green's function, following Geisler's (1970) approach. Finally, Nilsson (1995) used the linear solution written in the spectral space to calculate analytically the energy flux from a traveling tropical cyclone to the oceanic internal wave field.

However, in this work the focus is on nonlinearities, and it is shown that they break the analytical equivalence between a stratified ocean and the infinite set of shallow-water systems. Equation (6) projected on the lth internal mode gives

$$w_l = -\left(\frac{\partial u_l}{\partial x} + \frac{\partial v_l}{\partial y}\right). \tag{14}$$

The advective term can be brought to the right-hand side of Eq. (3) and then projected on the lth mode as follows:

$$\begin{aligned} -\left(u\frac{\partial}{\partial x} + v\frac{\partial}{\partial y} + w\frac{\partial}{\partial z}\right)u &= \sum_{n=1}^{+\infty}\left[-h_{nz}\left(u_n\frac{\partial}{\partial x} + v_n\frac{\partial}{\partial y}\right) + h_n\left(\frac{\partial u_n}{\partial x} + \frac{\partial v_n}{\partial y}\right)\frac{\partial}{\partial z}\right]\sum_{m=1}^{+\infty}(h_{mz}u_m) \\ &= \sum_{n,m=1}^{+\infty}\left[-h_{nz}h_{mz}\left(u_n\frac{\partial}{\partial x} + v_n\frac{\partial}{\partial y}\right) + h_n h_{mzz}\left(\frac{\partial u_n}{\partial x} + \frac{\partial v_n}{\partial y}\right)\right]u_m. \end{aligned} \tag{15}$$

Now the products $-h_{nz}h_{mz}$ and $h_n h_{mzz}$ can be decomposed on the basis of the modes for the horizontal velocity $\{h_{lz}\}_{l\in\mathbb{N}}$, so that

$$-h_{nz}h_{mz} = \sum_{l=0}^{+\infty}\alpha_{nml}h_{lz} \quad \text{and} \quad h_n h_{mzz} = \sum_{l=0}^{+\infty}\beta_{nml}h_{lz},$$

with the expansion coefficients given explicitly by

$$\alpha_{nml} = -\frac{\int_{-H}^{0} dz\, h_{nz}h_{mz}h_{lz}}{\int_{-H}^{0} dz\, h_{lz}^2}, \quad \text{and} \tag{16}$$

$$\beta_{nml} = \frac{\int_{-H}^{0} dz\, h_n h_{mzz}h_{lz}}{\int_{-H}^{0} dz\, h_{lz}^2}. \tag{17}$$

The same coefficients appear while projecting on the modes the v velocity component equation [Eq. (4)], so that the advective terms in the momentum equations are

$$-\left(u\frac{\partial}{\partial x} + v\frac{\partial}{\partial y} + w\frac{\partial}{\partial z}\right)u = \sum_{n,m,l=1}^{+\infty}\mathscr{U}_{nml}h_{lz}, \quad \text{and} \tag{18}$$

$$-\left(u\frac{\partial}{\partial x} + v\frac{\partial}{\partial y} + w\frac{\partial}{\partial z}\right)v = \sum_{n,m,l=1}^{+\infty}\mathscr{V}_{nml}h_{lz}, \tag{19}$$

with

$$\mathscr{U}_{nml} = \left[\alpha_{nml}\left(u_n\frac{\partial}{\partial x} + v_n\frac{\partial}{\partial y}\right) + \beta_{nml}\left(\frac{\partial u_n}{\partial x} + \frac{\partial v_n}{\partial y}\right)\right]u_m, \tag{20}$$

and

$$\mathscr{V}_{nml} = \left[\alpha_{nml}\left(u_n\frac{\partial}{\partial x} + v_n\frac{\partial}{\partial y}\right) + \beta_{nml}\left(\frac{\partial u_n}{\partial x} + \frac{\partial v_n}{\partial y}\right)\right]v_m. \tag{21}$$

Considering now the density equation [Eq. (7)], divided by the squared buoyancy frequency N^2, the coefficients

$$\lambda_{nml} = -\frac{c_l}{c_m}\frac{\int_{-H}^{0} dz\, N^2 h_{nz} h_m h_l}{\int_{-H}^{0} dz\, N^2 h_l^2}, \quad \text{and} \tag{22}$$

$$\mu_{nml} = -c_l c_m \frac{\int_{-H}^{0} dz\, h_n h_{mzzz} h_l}{\int_{-H}^{0} dz\, N^2 h_l^2} \tag{23}$$

are defined, so that one can write

$$-\frac{g}{\rho_o N^2}\left(u\frac{\partial}{\partial x} + v\frac{\partial}{\partial y} + w\frac{\partial}{\partial z}\right)\rho = \sum_{n,m,l=1}^{+\infty} \mathscr{R}_{nml}\frac{h_l}{c_l}, \tag{24}$$

with

$$\mathscr{R}_{nml} = \left[\lambda_{nml}\left(u_n\frac{\partial}{\partial x} + v_n\frac{\partial}{\partial y}\right) + \mu_{nml}\left(\frac{\partial u_n}{\partial x} + \frac{\partial v_n}{\partial y}\right)\right]\frac{g\eta_m}{c_m}. \tag{25}$$

The α_{nml}, β_{nml}, λ_{nml}, and μ_{nml} coefficients are calculated directly using their integral definitions introduced in Eqs. (16), (17), (22), and (23). They represent the geometrical equivalent of the well-known triangle condition for the vertical wavenumber

$$|k_z' \pm k_z''| = k_z''', \tag{26}$$

which is one of the necessary conditions for a triad interaction to be resonant. A triad is resonant, that is, it implies efficient energy exchange among the waves involved, when the conditions $\mathbf{k}' \pm \mathbf{k}'' = \mathbf{k}'''$ and $\omega' \pm \omega'' = \omega'''$ are satisfied (Phillips 1966; Thorpe 2005; Olbers et al. 2012). Appendix A shows that in the case of constant stratification the only nonzero coefficients are on the lines $|n \pm m| = l$, which strictly correspond to Eq. (26) since modenumbers are directly proportional to vertical wavenumbers.

By computing the above coefficients (not shown) it is clear that the effect of the variation of N with depth is to allow resonant interactions also out of the lines $|n \pm m| = l$ (Pomphrey et al. 1980), which is consistent with the fact that in the case of depth-varying stratification the local wavenumber of mode l varies with depth as $N(z)/c_l$, and thus there is no one-to-one correspondence between vertical wavenumbers and modenumbers. This, in turn, implies that the condition of Eq. (26) can be respected locally even if $|n \pm m| \neq l$.

Another interesting feature that characterizes the geometrical coefficients of the above is that only the α_{nml} ones are symmetrical under the exchange of the indices n and m, while all the others are not. This is part of the reason why also the $\mathscr{U}_{nml}$, $\mathscr{V}_{nml}$, and $\mathscr{R}_{nml}$ terms introduced above are not symmetrical under the n, m exchange. Thus, in the entire following discussion, one should keep in mind that the nth mode wave advects the mth mode one, and their roles are not interchangeable.

By introducing the variable $r_l = g\eta_l/c_l$, the set of governing equations [Eqs. (3)–(7)] can be projected on the lth internal mode as

$$\frac{\partial u_l}{\partial t} - f v_l + c_l\frac{\partial r_l}{\partial x} = \tau_l^x + \sum_{n,m}^{+\infty} \mathscr{U}_{nml}, \tag{27}$$

$$\frac{\partial v_l}{\partial t} + f u_l + c_l\frac{\partial r_l}{\partial y} = \tau_l^y + \sum_{n,m}^{+\infty} \mathscr{V}_{nml}, \quad \text{and} \tag{28}$$

$$\frac{\partial r_l}{\partial t} + c_l\left(\frac{\partial u_l}{\partial x} + \frac{\partial v_l}{\partial y}\right) = \sum_{n,m}^{+\infty} \mathscr{R}_{nml}, \tag{29}$$

together with the diagnostic equations $p_l = c_l r_l$ and $w_l = -(\partial u_l/\partial x + \partial v_l/\partial y)$.

It is known that the response of the ocean is steady in the frame of reference of the storm (Price 1981; Gill 1982), and thus, introducing the coordinate $\xi = x + Ut$, for a storm moving in the negative x direction, the derivatives change according to

$$\frac{\partial}{\partial x} = \frac{\partial \xi}{\partial x}\frac{\partial}{\partial \xi} = \frac{\partial}{\partial \xi} \quad \text{and} \quad \frac{\partial}{\partial t} = \frac{\partial \xi}{\partial t}\frac{\partial}{\partial \xi} = U\frac{\partial}{\partial \xi}.$$

The set of Eqs. (27)–(29) becomes

$$U\frac{\partial u_l}{\partial \xi} - f v_l + c_l\frac{\partial r_l}{\partial \xi} = \tau_l^x + \sum_{n,m}^{+\infty} \mathscr{U}_{nml}, \tag{30}$$

$$U\frac{\partial v_l}{\partial \xi} + f u_l + c_l\frac{\partial r_l}{\partial y} = \tau_l^y + \sum_{n,m}^{+\infty} \mathscr{V}_{nml}, \quad \text{and} \tag{31}$$

$$U\frac{\partial r_l}{\partial \xi} + c_l\left(\frac{\partial u_l}{\partial \xi} + \frac{\partial v_l}{\partial y}\right) = \sum_{n,m}^{+\infty} \mathscr{R}_{nml}, \tag{32}$$

with the appropriate replacements in the $\mathscr{U}_{nml}$, $\mathscr{V}_{nml}$, and $\mathscr{R}_{nml}$ terms as well.

While l varies from 1 to infinity, a small finite number of modes explains the majority of the total energy transferred to the ocean from the passing storm. To compare the relative importance of a single mode, the total energy of the initial set of equations [Eqs. (3)–(7)] is integrated vertically from the bottom to the top and decomposed as

$$\int_{-H}^{0} dz\, \frac{1}{2}\left(u^2 + v^2 + \frac{g^2\rho^2}{N^2\rho_o^2}\right) = \sum_{l=1}^{+\infty} \frac{1}{2}(u_l^2 + v_l^2 + r_l^2)\|h_{l_z}\|^2,$$

which applies because of the orthogonality of the modes. The squared norm $\|h_{lz}\|^2$ arises naturally in the solution of the Sturm–Liouville problem [Eq. (9)], and it is defined as

$$\|h_{lz}\|^2 = \int_{-H}^{0} dz\, h_{lz}^2. \tag{33}$$

The fields u, v, ρ are the ones obtained from the numerical simulations, and they are steady in the frame of reference of the storm; thus, they depend on (ξ, y, z) only. By introducing the 2D Fourier transform with wavenumbers k_x and k_y associated with the coordinates ξ and y, respectively, the spectral energy density for each mode can be defined. In particular, in the spectral domain, the steadiness condition for a storm moving in the negative x direction is

$$\omega = -k_x U, \tag{34}$$

which is a direct link between the frequency of the wave and the along-track wavenumber.

Since the Fourier transform [denoted with a hat (ˆ)] is a linear operator, then the spectral fields $\hat{u}$, $\hat{v}$, and $\hat{\rho}/\rho_o$ can also be expanded in the usual way

$$[\hat{u}, \hat{v}] = \sum_{l=1}^{+\infty} [\hat{u}_l, \hat{v}_l] h_{lz}, \quad \hat{\rho}/\rho_o = \sum_{l=1}^{+\infty} \hat{\eta}_l h_{lzz},$$

which leads to a similar decomposition on the modes for the power spectrum

$$\int_{-H}^{0} dz \frac{1}{2}\left(|\hat{u}|^2 + |\hat{v}|^2 + \frac{g^2|\hat{\rho}|^2}{N^2\rho_o^2}\right)$$
$$= \sum_{l=1}^{+\infty} \frac{1}{2}(|\hat{u}_l|^2 + |\hat{v}_l|^2 + |\hat{r}_l|^2)\|h_{lz}\|^2 = \sum_{l=1}^{+\infty} \hat{E}_l \|h_{lz}\|^2. \tag{35}$$

The spectral energy density for the lth mode, $\hat{E}_l(k_x, k_y) = (|\hat{u}_l|^2 + |\hat{v}_l|^2 + |\hat{r}_l|^2)/2$, is the spectral correspondent of the energy associated with the linear set of Eqs. (30)–(32). The above expression shows how energy is partitioned both in horizontal wavenumbers and in modenumbers. By denoting with a tilde the spectral variables integrated along the across-track wavenumber, namely,

$$\tilde{E}_l(k_x) = \int_{-\infty}^{+\infty} dk_y \hat{E}_l(k_x, k_y),$$

one can introduce the functions $\tilde{E}_l\|h_{lz}\|^2$, shown in the left panel of Fig. 4 for the first three modes. To study the stationary wake in the frame of reference of the storm starting from the numerical simulations, the projections of the wake on the internal modes are averaged by superimposing the center of the cyclone in the origin of the new frame of reference (ξ, y) at any given time. This reduces the transient response, which is not stationary in the frame of reference of the storm. A simple 2D Fourier transform is then applied to the steady wake. The near-inertial peak of the lth mode is around the Geisler wavenumber, which corresponds to the blue-shifted frequency of Eq. (13) through the steadiness condition [Eq. (34)]. From Fig. 4, it is clear that the most prominent blue shift appears in the first mode, as described by Gill (1982, chapter 9) in his linear theory.

The integral of the power spectrum around the near-inertial peak of the other modes ($l \geq 2$) monotonically decreases with the modenumber. This is equivalent to the near-inertial energy

$$\mathrm{NIE}(l) = \int_{I(f/U)} dk_x\, \tilde{E}_l \|h_{lz}\|^2 \tag{36}$$

decreasing monotonically except for the first mode, as shown in the right panel of Fig. 4. On the other hand, for the energy around the double-inertial peak,

$$\mathrm{DIE}(l) = \int_{I(2f/U)} dk_x\, \tilde{E}_l \|h_{lz}\|^2, \tag{37}$$

the first mode is the most energetic. The intervals of integration are chosen to be $I(f/U) = \{k_x \in \mathbb{R}: 0.8f/U < k_x < 1.6f/U\}$ and $I(2f/U) = \{k_x \in \mathbb{R}: 1.8f/U < k_x < 2.2f/U\}$, and they are shown as horizontal bars in the left panel of Fig. 4. Results are not sensitive to small changes in the choice of the intervals of integration.

The important point to emphasize is that, for NIE(l), the second mode dominates, tightly followed by the third mode, while for DIE(l) it is the first one that has most of the energy. Therefore, because of the fast decrease of the DIE(l), the analysis is limited to consideration of the first three:
$l = 1, 2, 3$.

4. Analytical spectral decomposition

By writing down the nonlinear projected equations in the spectral domain, it is possible to quantify analytically the relative contribution of the linear forcing and the nonlinear advection terms to the energy around the double-inertial frequency of the first three modes.

In Fourier space, Eqs. (30)–(32) become

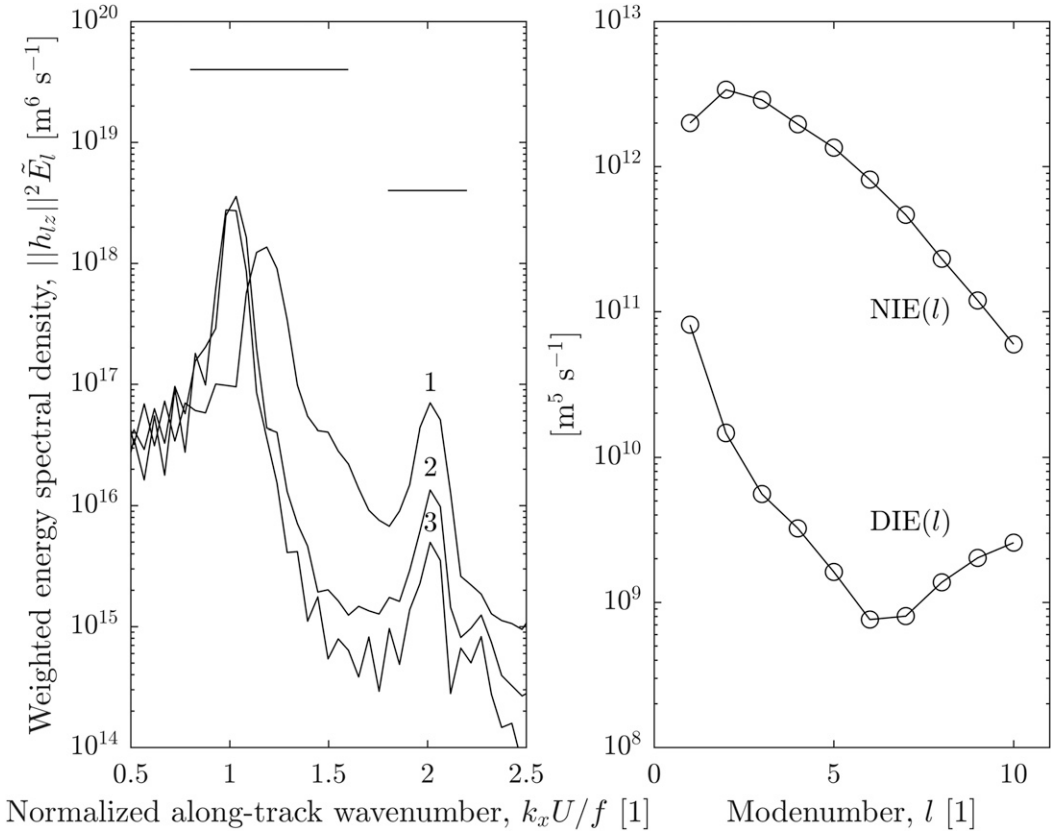

FIG. 4. (left) The first three weighted power spectra $\|h_{lz}\|^2\tilde{E}_l(k_x)$ with $l = 1, 2, 3$ obtained from the simulation D8000. The tilde is used to denote spectral variables integrated along the across-track wavenumber, and the squared norm of the mode is the weight needed to correctly compare the contribution of each mode. (right) The horizontal bars show the intervals of integration used to define the near-inertial energy NIE(l) of Eq. (36), and the double-inertial energy DIE(l) of Eq. (37), shown as a function of the modenumber. It is important to notice that the second and the third mode are the most energetic in terms of NIE(l), but it is the first one that contains most of the DIE(l).

$$ik_xU\hat{u}_l - f\hat{v}_l + ik_xc_l\hat{r}_l = \hat{\tau}_l^x + \sum_{n,m}^{+\infty}\hat{\mathscr{U}}_{nml}, \tag{38}$$

$$ik_xU\hat{v}_l + f\hat{u}_l + ik_yc_l\hat{r}_l = \hat{\tau}_l^y + \sum_{n,m}^{+\infty}\hat{\mathscr{V}}_{nml}, \quad \text{and} \tag{39}$$

$$ik_xU\hat{r}_l + c_l(ik_x\hat{u}_l + ik_y\hat{v}_l) = \sum_{n,m}^{+\infty}\hat{\mathscr{R}}_{nml}, \tag{40}$$

which can be rewritten in matrix form as $\mathbf{A}\hat{\mathbf{x}} = \hat{\mathbf{b}}$ with

$$\mathbf{A} = \begin{bmatrix} ik_xU & -f & ik_xc_l \\ f & ik_xU & ik_yc_l \\ ik_xc_l & ik_yc_l & ik_xU \end{bmatrix}, \quad \hat{\mathbf{x}} = \begin{pmatrix} \hat{u}_l \\ \hat{v}_l \\ \hat{r}_l \end{pmatrix},$$

$$\hat{\mathbf{b}} = \hat{\mathbf{b}}_o + \sum_{n,m}^{+\infty}\begin{pmatrix} \hat{\mathscr{U}}_{nml} \\ \hat{\mathscr{V}}_{nml} \\ \hat{\mathscr{R}}_{nml} \end{pmatrix}, \quad \hat{\mathbf{b}}_o = \begin{pmatrix} \hat{\tau}_l^x \\ \hat{\tau}_l^y \\ 0 \end{pmatrix}. \tag{41}$$

With this notation, it is straightforward to calculate the spectral energy density for the lth mode as

$$\hat{E}_l = \frac{1}{2}(|\hat{u}_l|^2 + |\hat{v}_l|^2 + |\hat{r}_l|^2) = \frac{1}{2}[\hat{\mathbf{b}}^{*\mathrm{T}}(\mathbf{A}\mathbf{A}^{*\mathrm{T}})^{-1}\hat{\mathbf{b}}], \tag{42}$$

where the star * denotes the complex conjugate, and the superscript $^{\mathrm{T}}$ denotes the transpose. With the definition of the matrix $\mathbf{C} = (\mathbf{A}\mathbf{A}^{*\mathrm{T}})^{-1}$, one finds

$$\hat{E}_l = \frac{1}{2}(C_{11}|\hat{b}_1|^2 + C_{22}|\hat{b}_2|^2 + C_{33}|\hat{b}_3|^2) + \mathrm{Re}\{C_{12}\hat{b}_1^*\hat{b}_2 + C_{13}\hat{b}_1^*\hat{b}_3 + C_{23}\hat{b}_2^*\hat{b}_3\}. \tag{43}$$

The coefficients C_{ij} are polynomials in the variables k_x, k_y, and they are explicitly written in appendix B. By replacing the forcing vector $\mathbf{b}$ of Eq. (41) in Eq. (42), the spectral energy density becomes

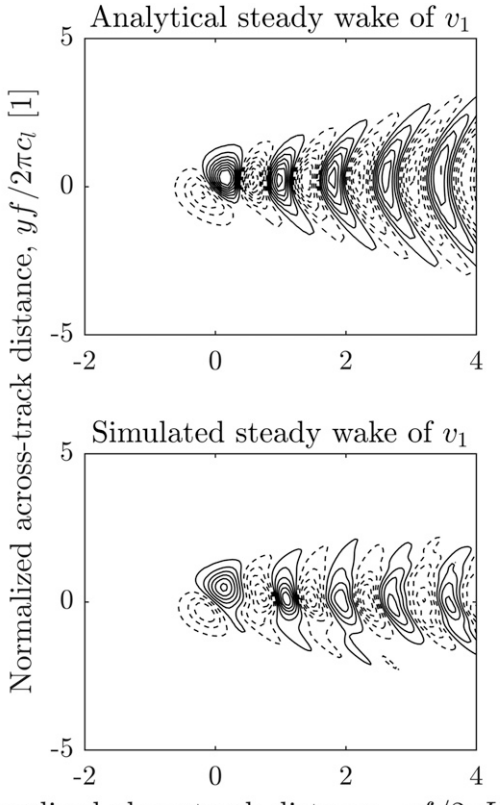

FIG. 5. Steady wave wake of the v velocity component projected on the first internal mode. The contour lines go from -0.15 to $0.15\,\mathrm{m\,s^{-1}}$ with interval of $0.02\,\mathrm{m\,s^{-1}}$. Solid contours are for positive values, and dashed contours are for negative ones. The along-track distance from the center of the storm is normalized by the inertial wavelength $2\pi U/f$, while the across-track distance is normalized by the wavelength associated with the baroclinic radius of deformation, that is, $2\pi c_l/f$.

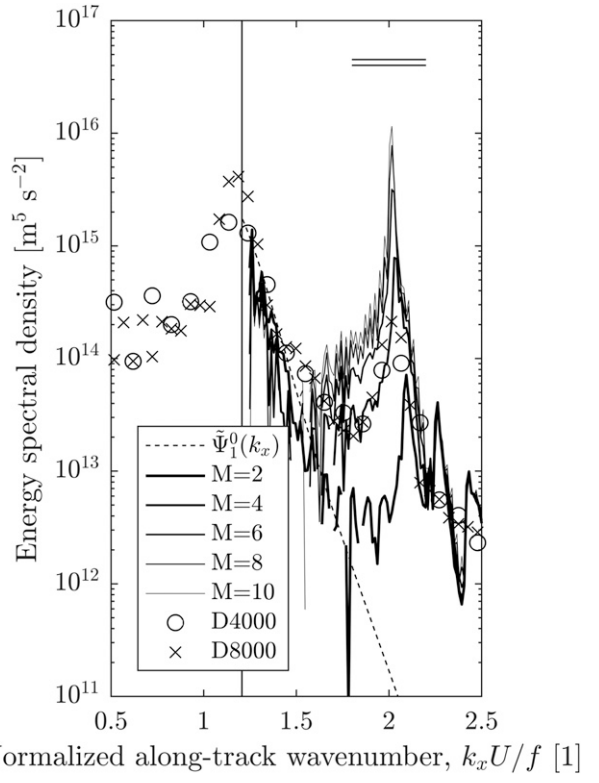

FIG. 6. The dashed line shows the linear spectrum $\tilde{\Psi}_l^0(k_x)$ with $l = 1$. The solid lines show the truncated energy spectral density $\tilde{E}_l^{(M)}(k_x)$, as in Eq. (55), for various values of M. The peak near $k_xU/f = 2$ increases with increasing M. The circles show the total energy spectral density $\tilde{E}_l(k_x)$ obtained from the simulation D4000 and the crosses from the simulation D8000. The horizontal double line marks the interval of integration $I(2f/U)$ of Eq. (53).

$$\hat{E}_l(k_x,k_y) = \Psi_l^0 + \sum_{n,m=1}^{+\infty} \Psi_{nml}^1 + \sum_{q,s,n,m=1}^{+\infty} \Psi_{qsnml}^2, \tag{44}$$

where

$$\Psi_l^0(k_x,k_y) = \frac{1}{2}(C_{11}|\hat{\tau}_l^x|^2 + C_{22}|\hat{\tau}_l^y|^2) + \mathrm{Re}\{C_{12}(\hat{\tau}_l^x)^*\hat{\tau}_l^y\} \tag{45}$$

contains no advection term,

$$\begin{aligned}\Psi_{nml}^1(k_x,k_y) = {} & \mathrm{Re}\{[C_{11}(\hat{\tau}_l^x)^* + C_{12}^*(\hat{\tau}_l^y)^*]\hat{\mathscr{U}}_{nml}\} \\ & + \mathrm{Re}\{[C_{12}(\hat{\tau}_l^x)^* + C_{22}(\hat{\tau}_l^y)^*]\hat{\mathscr{V}}_{nml}\} \\ & + \mathrm{Re}\{[C_{13}(\hat{\tau}_l^x)^* + C_{23}(\hat{\tau}_l^y)^*]\hat{\mathscr{R}}_{nml}\}\end{aligned} \tag{46}$$

contains advection terms to the first power, and

$$\begin{aligned}\Psi_{qsnml}^2(k_x,k_y) = {} & \frac{1}{2}(C_{11}\mathrm{Re}\{\hat{\mathscr{U}}_{qsl}^*\hat{\mathscr{U}}_{nml}\} + C_{22}\mathrm{Re}\{\hat{\mathscr{V}}_{qsl}^*\hat{\mathscr{V}}_{nml}\} \\ & + C_{33}\mathrm{Re}\{\hat{\mathscr{R}}_{qsl}^*\hat{\mathscr{R}}_{nml}\}) + \mathrm{Re}\{C_{12}\hat{\mathscr{U}}_{qsl}^*\hat{\mathscr{V}}_{nml} \\ & + C_{13}\hat{\mathscr{U}}_{qsl}^*\hat{\mathscr{R}}_{nml} + C_{23}\hat{\mathscr{V}}_{qsl}^*\hat{\mathscr{R}}_{nml}\}\end{aligned} \tag{47}$$

contains products of two advection terms.

To focus on the energy exchanges involving the double-inertial frequency range, one can make use of the steadiness condition [Eq. (34)] that relates directly the along-track wavenumber to the frequency. Denoting with a tilde the functions integrated along the k_y axis, one obtains the power spectrum density and its components as a function of the along-track wavenumber only, namely,

$$\tilde{E}_l(k_x) = \tilde{\Psi}_l^0 + \sum_{n,m=1}^{+\infty} \tilde{\Psi}_{nml}^1 + \sum_{q,s,n,m=1}^{+\infty} \tilde{\Psi}_{qsnml}^2. \tag{48}$$

These integrals are defined as the Cauchy principal value, as explained precisely in appendix B.

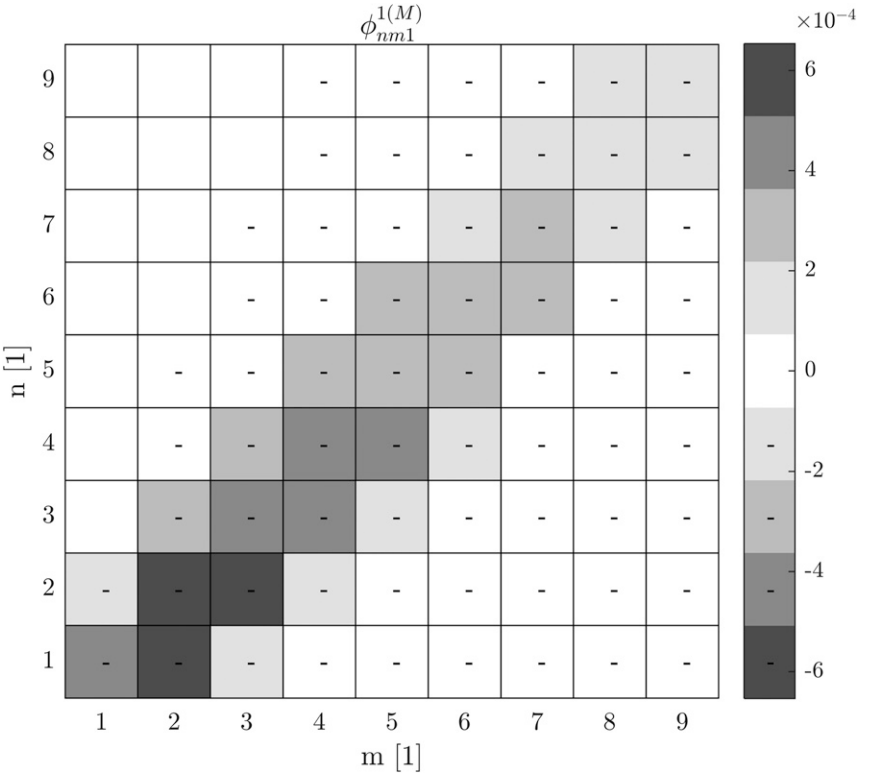

FIG. 7. The $\phi^{1(M)}_{nml}$ coefficients for $M = 10$, $n, m \in [1, 10]$, and $l = 1$. The minus denotes negative values.

The final step to have a simple measure of the relative importance of a certain interaction of waves in the generation of the double-inertial energy peak of the lth wave is to integrate the previous equation around the value $k_x = 2f/U$. In particular, the following coefficients can be defined:

$$\varepsilon_l = \int_{I(2f/U)} dk_x \, \tilde{E}_l, \tag{49}$$

$$\phi^0_l = \frac{1}{\varepsilon_l} \int_{I(2f/U)} dk_x \, \tilde{\Psi}^0_l, \tag{50}$$

$$\phi^1_{nml} = \frac{1}{\varepsilon_l} \int_{I(2f/U)} dk_x \, \tilde{\Psi}^1_{nml}, \quad \text{and} \tag{51}$$

$$\phi^2_{qsnml} = \frac{1}{\varepsilon_l} \int_{I(2f/U)} dk_x \, \tilde{\Psi}^2_{qsnml}, \tag{52}$$

where

$$I(2f/U) = \{k_x \in \mathbb{R}: 2f/U - \Delta k_x \le k_x \le 2f/U + \Delta k_x\}, \tag{53}$$

with an appropriate Δk_x. As for the calculation of the DIE(l) of Eq. (37), $\Delta k_x = 0.2f/U$, and it was checked that the results are not sensitive to small changes in the choice of this value, as far as only the double-inertial peak is included in the integrals. Thanks to these definitions, Eq. (48) becomes

$$1 = \phi^0_l + \sum_{n,m=1}^{+\infty} \phi^1_{nml} + \sum_{q,s,n,m=1}^{+\infty} \phi^2_{qsnml}, \tag{54}$$

and each of the three addenda express the relative contribution of linear, first-order advection and second-order advection terms to the energy of mode l in the double-inertial range.

To show the results, all the series that appear in Eqs. (48) and (54) are stopped at a certain modenumber M, so that the truncated energy spectral density is defined as

$$\tilde{E}^{(M)}_l(k_x) = \tilde{\Psi}^0_l + \sum_{n,m=1}^{M} \tilde{\Psi}^1_{nml} + \sum_{q,s,n,m=1}^{M} \tilde{\Psi}^2_{qsnml}, \tag{55}$$

which leads to the definition of the truncated double-inertial energy

$$\varepsilon^{(M)}_l = \int_{I(2f/U)} dk_x \, \tilde{E}^{(M)}_l \tag{56}$$

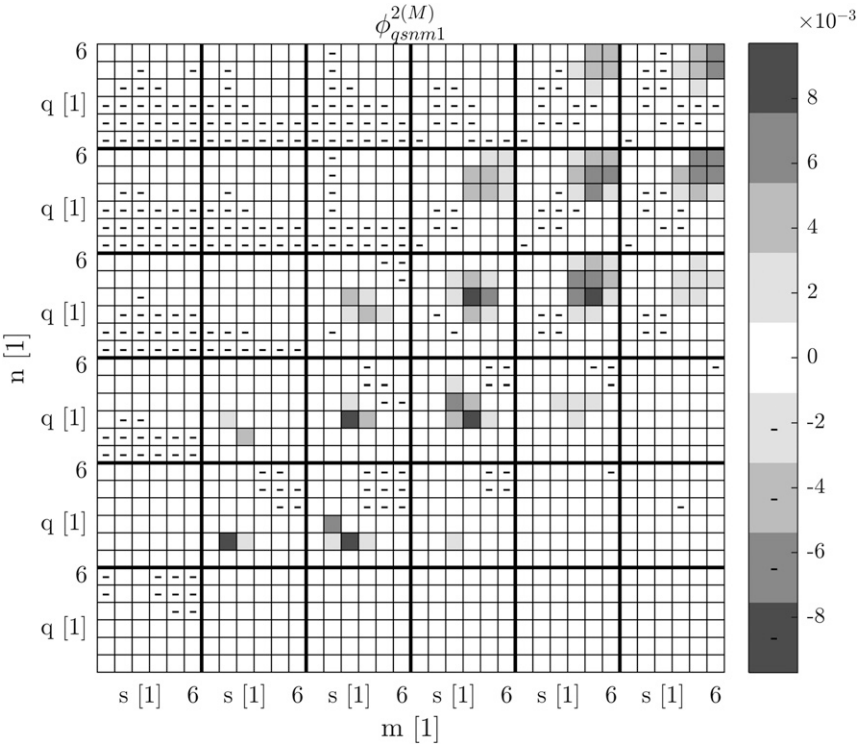

FIG. 8. The $\phi^{2(M)}_{qsnml}$ coefficients for $M = 10$, $q, s \in [1, 6]$, $n, m \in [1, 6]$, and $l = 1$. The minus denotes negative values.

and the truncated coefficients $\phi^{0(M)}_{l}$, $\phi^{1(M)}_{nml}$, and $\phi^{2(M)}_{qsnml}$. Those are defined as in Eqs. (50)–(52) with $\varepsilon^{(M)}_{l}$ instead of ε_l, which means that Eq. (54) holds even for these coefficients.

5. Results

The quantities shown in this section are calculated analytically, starting from the linear solutions obtained by transforming the spectral variables

$$\hat{\mathbf{x}} = \mathbf{A}^{-1}\hat{\mathbf{b}}_o \tag{57}$$

back to the physical space, as explained in detail in appendix C. The truncated coefficients $\phi^{0(M)}_{l}$, $\phi^{1(M)}_{nml}$, and $\phi^{2(M)}_{qsnml}$, that satisfy

$$1 = \phi^{0(M)}_{l} + \sum_{n,m=1}^{M} \phi^{1(M)}_{nml} + \sum_{q,s,n,m=1}^{M} \phi^{2(M)}_{qsnml} \tag{58}$$

thus measure the energy transfer between modes due to the nonlinear interactions of the linear solutions. In particular, they measure the energy exchanged between the lth-mode, double-inertial peak and the qth, sth, nth, and mth waves.

The analytical solutions are computed on a bigger grid compared to the one used in the numerical simulation to have a finer wavenumber step. The grid is 64×10^3 km long in the longitudinal direction and 24×10^3 km in the latitudinal one, with grid spacing $\Delta x = \Delta y = 80$ km. Figure 5 shows the wave wake for the first projection of the v field calculated analytically (upper panel) and obtained from the numerical simulation (lower panel). Once the linear u_l, v_l, r_l are known for many l, one can compute the advection terms of Eqs. (20), (21), and (25) and then the spectral functions of Eqs. (45)–(47). The integrals along k_y (as explained in appendix B) and the integrals around the double-inertial peak are finally performed to find the truncated coefficients of Eq. (58).

As shown in Fig. 6, the net effect of nonlinear interactions is to add energy to the double-inertial range. In the same figure, one can also see that the variation of M in the range [6, 10] does not influence the position of the double-inertial peak. Its height changes because more and more interactions are taken into consideration, and, in the analytical solution, they are all certainly happening. Thus, compared to the numerical spectra, the analytical solution gives an upper bound to the height of the

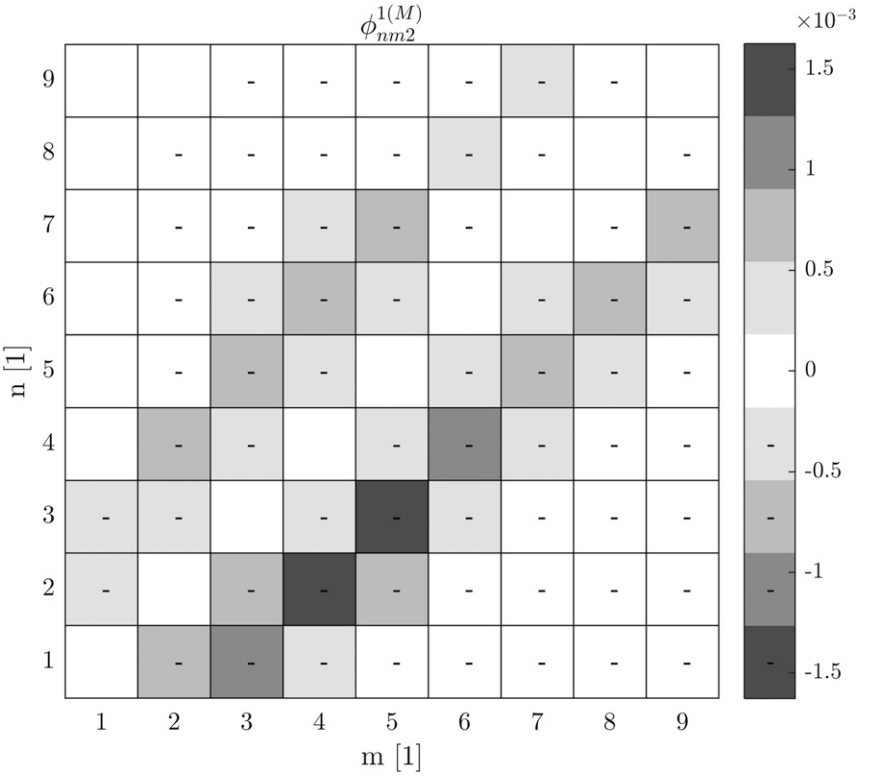

FIG. 9. As in Fig. 7, but for $l = 2$.

double-inertial peak in the case that all possible interactions among the waves in the wake behind the storm are exchanging energy. The peaks in the D8000 spectrum are higher than the D4000 ones both because the domain is larger (the D8000 domain is twice as large as the D4000 one) and because more wave interactions happen and bring energy to the double-inertial peak.

To quantify the role of the single interaction of waves in the generation of the double-inertial peak, the coefficients $\phi^{1(M)}_{nml}$ are shown in Fig. 7 for $M = 10$, $n, m \in [1, 10]$, and the coefficients $\phi^{2(M)}_{qsnml}$ in Fig. 8 for $M = 10$, $n, m \in [1, 6]$, and $q, s \in [1, 6]$. Positive values correspond to nonlinear interactions that bring energy to the lth-mode, double-inertial peak from the interacting waves, while negative values correspond to interactions that take energy away from the lth-mode, double-inertial peak. There is no balance between the sum of all the positive coefficients and the negative ones because that would correspond to a zero net contribution of the nonlinear interactions in the generation of the double-inertial peak and to an energy spectral distribution decaying as $\tilde{\Psi}^0_l(k_x)$, that is, with no double-inertial peak. A total zero sum could be expected if the coefficients under study were energy exchange rates and not integrated energy transfer, as they are in the present work.

The following figures, Figs. 9–12, confirm the description of the energy exchanges between near-inertial and double-inertial waves of different modes by showing the same coefficients $\phi^{1(M)}_{nml}$ and $\phi^{2(M)}_{qsnml}$ for $l = 2$ and $l = 3$. In this way, some general features can be drawn. First of all, the geometrical constraint due to the structure of the α_{nml}, β_{nml}, λ_{nml}, and μ_{nml} coefficients, that is, the triangle condition on the modenumbers, appears in all the cases. In particular, the dominant coefficients in Figs. 7–12 are always the one with ($n = 2$ or 3 and $m = l + n$) or ($q = 2$ or 3, $s = l + q$, $n = 2$ or 3, and $m = l + n$). It was proved that the entire interpretation of the mechanism does not depend on the value of M, as far as it is high enough to capture the dominant interaction for the selected mode. This means that for the first three modes, the Figs. 7–12 are qualitatively the same for $M \in [6, 10]$, in the sense that the relative importance of the coefficients with respect to one another is independent of M.

The same coefficients of Figs. 7–12 were calculated using the waves simulated in D4000 and D8000, and very small differences with the coefficients shown here were found, of the order of a few percentage points (not

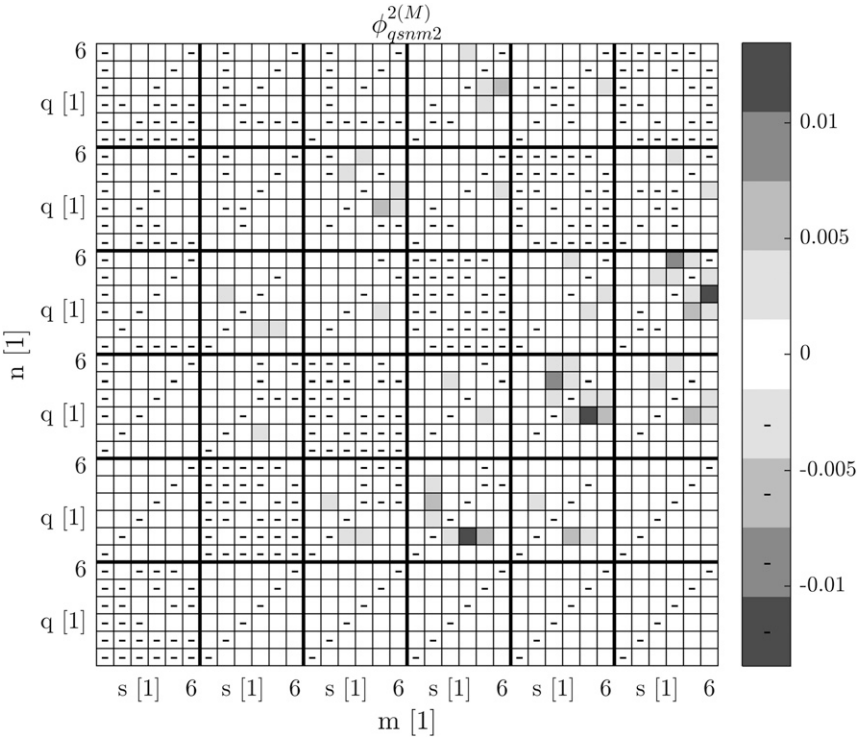

FIG. 10. As in Fig. 8, but for $l = 2$.

shown). This means that the presence of some energy in the double-inertial range of the interacting waves does not influence the picture of the mechanism outlined above.

6. Discussion and conclusions

The generation mechanism of the double-inertial frequency waves is analyzed using the internal mode decomposition and defining analytically the coefficients of Eqs. (51) and (52) that measure the relative importance of the contribution of the interacting modes (qth, sth, nth, and mth) to the double-inertial frequency range of the power spectrum of the reference mode l. The analytical theory developed in this work describes the nonlinear interactions of the linear solutions of the problem, which are compared to the fully nonlinear solutions obtained from two numerical simulations. This gives a more detailed view of the process compared to previous works (Niwa and Hibiya 1997; Danioux and Klein 2008; Zedler 2009) in a realistic setting with a nonuniform oceanic stratification profile, and it highlights the role played by superinertial waves to ocean interior mixing.

First of all, let us comment on the apparent discrepancy between Niwa and Hibiya's (1997) and Zedler's (2009) identification of the depth at which nonlinear interactions take place. In the present work, it is found that the relatively dominant interactions that bring energy to the low-modenumber, double-inertial range waves generally involve a second- or third-mode wave ($n = 2$ or 3). This suggests that nonlinear interactions are important where the second and third modes peak, that is, in the range 1000–2500 m for the h_n modes and in the region of 500–750 m for the h_{nz} modes (see Fig. 3). As pointed out in the introduction, according to a WKB-like scaling, the energy should scale vertically as the buoyancy frequency profile and thus most of the energy exchanges would take place at the base of the mixed layer (see Fig. 2). Thus, the present analysis supports the idea that Niwa and Hibiya (1997) and Zedler (2009) interpretations of the depths at which nonlinear interactions take place is different simply because they use different vertical buoyancy frequency profiles but also that a simple WKB-like scaling would underestimate the depth at which nonlinear interactions are important.

Moreover, concerning the first mode ($l = 1$), which contains most of the double-inertial frequency energy, Fig. 8 proves that high-mode, near-inertial energy is transferred to the first-mode, double-inertial peak, which is consistent with the results of Niwa and Hibiya (1997). As shown in appendix D, this corresponds to a faster lateral energy propagation speed and must be

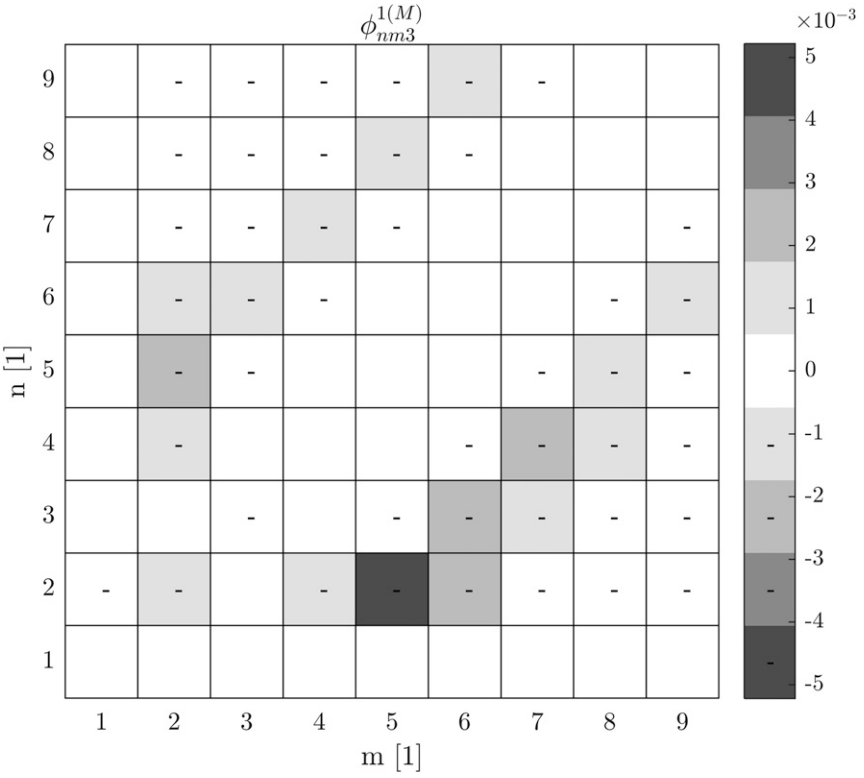

FIG. 11. As in Fig. 7, but for $l = 3$.

taken into account when studying the radiation of energy from a wake excited by a tropical cyclone. In particular, in appendix D a sufficient condition for having an increase of the lateral energy propagation speed during the transfer of energy from a high-mode, near-inertial wave to a low-mode, double-inertial one for an exponential stratification, $N(z) = N_o e^{z/\lambda}$ with $z \in [-H, 0]$, is derived. Such a sufficient condition states that the cyclone translation speed U must exceed the threshold value $\overline{U}_{2,1} \simeq \lambda N_o \times 10^{-1}$. Considering as upper bound the values $N_o \simeq 10^{-2}\,\mathrm{s}^{-1}$ and $\lambda \simeq 10^3\,\mathrm{m}$ (Pickard and Emery 1990), one finds $\overline{U}_{2,1} \simeq 1\,\mathrm{m\,s}^{-1}$, which means that for nearly all the tropical cyclones that generally move with a translation speed between 1 and $10\,\mathrm{m\,s}^{-1}$, the transfer of energy from a high-mode m near-inertial range to a low-mode l double-inertial range corresponds to an increase of the lateral energy propagation speed. Since, considering $l = 1, 2, 3$, this kind of transfer is very common (in correspondence of all the positive values of Figs. 7–12), nonlinearities account for an increase of the lateral energy propagation speed from the wake excited by a tropical cyclone.

On the other hand, the presence of negative values in Figs. 7–12 (in particular in Figs. 7, 9, and 11) shows energy flowing from the double-inertial range of mode l to some higher-mode n, $m > l$. This is in agreement with the possibility of a parametric subharmonic instability mechanism acting in the wave wake (McComas and Müller 1981), and since this energy is going toward high modes, these figures explicitly show a step in the cascade toward small scales, where the mixing happens.

Thus, the complete underlying mechanism that is found and that is in full agreement with the recent results of Wagner and Young (2016) can be summarized in a few steps:

- the wind stress inputs energy in the near-inertial range of all vertical modes;
- nonlinear interactions bring part of this energy toward the double-inertial range (which means that the waves are less likely to undergo critical latitude reflection) of the lowest modes (which have a higher horizontal group speed); and
- the double-inertial energy, which has been brought farther and faster compared to a purely linear system, is transferred back to the near-inertial range of some high vertical mode, that is, energy flows toward the small mixing scales.

In the present work, the temporal evolution of the nonlinear interactions has not been analyzed, as the

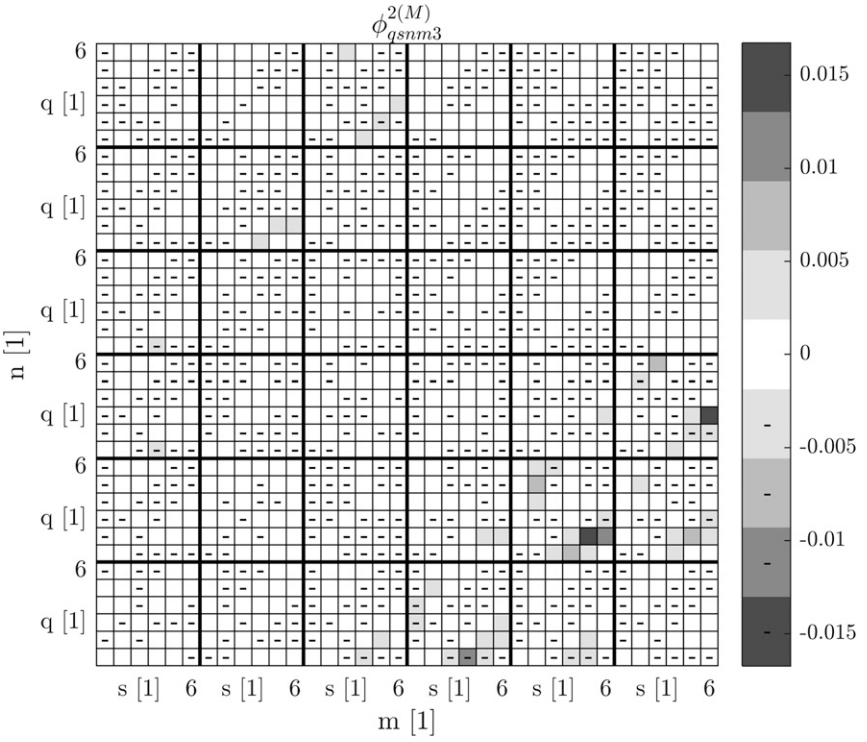

FIG. 12. As in Fig. 8, but for $l = 3$.

focus has been on the equilibrated oceanic response. It would be interesting to study in a future work the time constant for such equilibrated state to be reached.

Acknowledgments. A. N. M. is funded by the Flagship Project RITMARE—the Italian Research for the Sea—coordinated by the Italian National Research Council and funded by the Italian Ministry of Education, University and Research within the National Research Program 2011-2013 and by the EXTRA exchange program 2012-2013 of the University of Milan-Bicocca. M. D. M. and E. T. are supported by NASA ROSES Grant NNX14AH39G. E. T. is supported by NSF Physical Oceanography Grant OCE-1535800 and thanks the Weizmann Institute for its hospitality during parts of this work. The authors are grateful for the careful revision of the anonymous reviewers, which lead to substantial improvements of the manuscript.

APPENDIX A

Constant Stratification

The solutions of the Sturm–Liouville problem [Eq. (9)] in the case of constant stratification, that is, when $N = N_o$, are

$$h_n(z) = \frac{H}{n\pi}\sin\left(\frac{n\pi}{H}z\right), \quad \text{and}$$
$$h_{nz}(z) = \cos\left(\frac{n\pi}{H}z\right),$$

which means that the vertical wavenumber is directly proportional to the modenumber. The eigenspeeds are given by $c_n = HN_o/n\pi$, which means that $c_n \sim n^{-1}$. Then, for $n, m, l \geq 1$, the definitions from Eqs. (16), (17), (22), and (23) give analytically

$$\alpha_{nml} = -\frac{1}{2\pi}(\delta_{n+m,l} + \delta_{n-m,l} + \delta_{-n+m,l}), \tag{A1}$$

$$\beta_{nml} = \frac{1}{2\pi}\frac{m}{n}(\delta_{n+m,l} - \delta_{n-m,l} - \delta_{-n+m,l}), \tag{A2}$$

$$\lambda_{nml} = \frac{1}{2\pi}(-\delta_{n+m,l} + \delta_{n-m,l} - \delta_{-n+m,l}), \quad \text{and} \tag{A3}$$

$$\mu_{nml} = \frac{1}{2\pi}\frac{m}{n}(\delta_{n+m,l} + \delta_{n-m,l} - \delta_{-n+m,l}), \tag{A4}$$

where the Kronecher delta appears, and it imposes that the nonzero coefficients are only on the lines $n = m \pm l$ and $n = -m + l$. These relations, since the vertical wavenumber is directly proportional to the modenumber, represent simply the triangle condition for the vertical wavenumber [Eq. (26)]. That is why the α_{nml}, β_{nml}, λ_{nml}, and μ_{nml} coefficients can be interpreted as the

geometrical equivalent in the modenumber space of the triangle condition [Eq. (26)].

APPENDIX B

Power Spectrum Matrix

The matrix $\mathbf{C} = (\mathbf{A}\mathbf{A}^{*\mathrm{T}})^{-1}$ appears in Eq. (43). Since $\mathbf{A}$ is anti-Hermitian, it follows that $\mathbf{C} = -(\mathbf{A}\mathbf{A})^{-1}$ holds as well. To find the inverse of $-\mathbf{A}\mathbf{A}$, one first writes the determinant of $-\mathbf{A}\mathbf{A}$ with the Binet theorem,

$$\begin{aligned}\det(-\mathbf{A}\mathbf{A}) &= \det(-\mathbb{I})[\det(\mathbf{A})]^2 \\ &= k_x^2U^2[k_x^2(U^2-c_l^2) - k_y^2c_l^2 - f^2]^2, \end{aligned} \tag{B1}$$

where $\mathbb{I}$ is the identity matrix, and then, with the cofactors method, the entries of the inverse matrix are

$$C_{11}(k_x,k_y) = \frac{1}{k_x^2U^2} + \frac{f^2+c_l^2k_x^2}{k_x^2U^2}W + 2(f^2+c_l^2k_x^2)W^2, \tag{B2}$$

$$C_{22}(k_x,k_y) = \frac{1}{k_x^2U^2} + \frac{f^2+c_l^2k_y^2}{k_x^2U^2}W + 2(f^2+c_l^2k_y^2)W^2, \tag{B3}$$

$$C_{33}(k_x,k_y) = \frac{1}{k_x^2U^2} + \frac{c_l^2(k_x^2+k_y^2)}{k_x^2U^2}W + 2c_l^2(k_x^2+k_y^2)W^2, \tag{B4}$$

$$C_{12}(k_x,k_y) = \frac{k_yc_l^2}{k_xU^2}W + 2(k_xk_yc_l^2 - ifk_xU)W^2, \tag{B5}$$

$$C_{13}(k_x,k_y) = \frac{ifk_yc_l}{k_x^2U^2}W + 2(-k_x^2Uc_l + ifk_yc_l)W^2, \quad \text{and} \tag{B6}$$

$$C_{23}(k_x,k_y) = -\frac{ifc_l}{k_xU^2}W - 2(k_xk_yUc_l + ifk_xc_l)W^2, \tag{B7}$$

with

$$W(k_x,k_y) = \frac{1}{U^2k_x^2 - f^2 - c_l^2(k_x^2+k_y^2)} \in \mathbb{R}. \tag{B8}$$

As Nilsson (1995) explains very well, the locus of wavenumbers defined by the zero of the denominator of the above function selects the waves that can move steadily with the storm. This, in the present work, means that only waves whose wavenumber (k_x, k_y) belongs to the hyperbola

$$U^2k_x^2 = f^2 + c_l^2(k_x^2+k_y^2) \tag{B9}$$

are considered in the energy exchanges. As a consequence, this excludes that the second harmonic peak is phase locked to the fundamental peak, which is the one centered on the Geisler wavenumber

$$\mathbf{k}_{Gl} = \left(\frac{f}{\sqrt{U^2-c_l^2}}, 0\right). \tag{B10}$$

In fact, the wavenumber of a second harmonic phase-locked wave is the double of the Geisler wavenumber $\mathbf{k}_{2,p.l.} = 2\mathbf{k}_{Gl}$, which one can easily verify that does not belong to the hyperbola of the above.

Then, both when finding the solutions of the linear problem, as in appendix C, and when integrating Eqs. (45)–(47) along the across-track wavenumber k_y, the zeros in the denominator of the function $W(k_x, k_y)$ make it necessary to regularize the integrals by taking their Cauchy principal value, denoted with a P in front of them. The general form of such integrals is then

$$\begin{aligned} &P\int_{-\infty}^{\infty} ds\, f(s)\frac{s^\gamma}{D^\nu} \quad \text{with} \\ &D = (s-\chi)(s+\chi)(s-\chi^*)(s+\chi^*), \end{aligned} \tag{B11}$$

where $\chi \in \mathbb{C}$ is a first-order pole, and $f(s)$ is a smooth regular function that decays fast enough as s increases, so that the Jordan's lemma and the residues theorem can be applied. Note that the fact that $\mathrm{Im}\{\chi\} \neq 0$ is a consequence of the introduction of a small imaginary parameter that mimics some form of dissipation in the equations of motion. This is necessary only while calculating the linear analytical solution in order to overcome the famous mathematical ambiguity discussed in appendix D (Lighthill 1978, chapter 3). Back to the integrals of Eq. (B11), remember that the real function $f(s)$ of a real variable s can always be decomposed as a sum of its even part and its odd one, that is, $f(s) = f_E(s) + f_O(s)$, with $f_E(s) = [f(s) + f(-s)]/2$ and $f_O(s) = [f(s) - f(-s)]/2$. This means that in the integral (B11) only one of the two gives a nonzero contribution according to the parity of $f(s)s^\gamma$. The ranges of parameters needed in this work are $\gamma \in [0, 6] \subset \mathbb{N}$ and $\nu \in [1, 2] \subset \mathbb{N}$ and come from the structure of the C_{ij} polynomials introduced above.

By Fourier transforming along s, which corresponds to decompose the function on the Fourier basis $\{e^{isk}\}_{k\in\mathbb{R}}$, and by extending the integral in the complex s plane, the path of integration can be correctly closed in the upper half plane or in the lower one following the Jordan's lemma. With the definition of

$$f(s) = \frac{1}{\sqrt{2\pi}}\int_{-\infty}^{+\infty} dk\, e^{iks}\hat{f}(k) \tag{B12}$$

and a little algebra, the residues theorem gives

$$P\int_{-\infty}^{\infty} ds f(s)\frac{s^{\gamma}}{D^{\nu}} = 2i\sqrt{2\pi}\int_{0}^{+\infty} dk\,\hat{f}(k)\sum_{\mathrm{UP}}\mathrm{Res}\left\{\frac{s^{\gamma}e^{iks}}{D^{\nu}}\right\}, \tag{B13}$$

where UP denotes the upper half plane corresponding to $\mathrm{Im}\{s\} > 0$. The advantage of this approach is that the residues that appear in the last equation can be calculated analytically, while the form of the function $f(s)$ may not be known analytically.

APPENDIX C

Linear Analytical Solution

While solving the linear problem, a famous mathematical ambiguity arises. It comes from the fact that the mathematical problem includes wave solutions coming from infinity, but the physical problem describes waves excited by the forcing acting in the domain considered. This ambiguity can be solved by adding an imaginary part to the wavenumber k_x (in this problem this is achieved by replacing k_x with $k_x - i\delta$, $\delta > 0$) before inverting the Fourier integrals and then by taking the limit where the imaginary part goes to zero (Lighthill 1978, chapter 3). Formally, using the symbols of Eq. (41), the linear solutions are

$$\mathbf{x} = \begin{pmatrix} u_l \\ v_l \\ r_l \end{pmatrix} = \lim_{\delta\to 0}\frac{1}{2\pi}\int\int_{-\infty}^{\infty} dk_x\,dk_y\,\mathrm{e}^{i(k_x\xi + k_y y)}\hat{\mathbf{x}}(k_x - i\delta, k_y), \tag{C1}$$

where

$$\hat{\mathbf{x}}(k_x - i\delta, k_y) = (\mathbf{A}^{-1}\hat{\mathbf{b}}_o)\big|_{k_x = k_x - i\delta}. \tag{C2}$$

While inverting the Fourier integral of the above, the technique introduced in appendix B is used. As an example, the linear solution for v_l is written as

$$v_l(\xi, y) = \frac{1}{\sqrt{2\pi}}\int_{-\infty}^{+\infty} dk_y\left\{\frac{1}{U^2 - cl^2}\left[-\frac{k_y c_l^2}{U}\cos(k_y y) + f\sin(k_y y)\right]J(\xi, k_y) + \frac{\cos(k_y y)}{U}Y(\xi, k_y)\right\}, \tag{C3}$$

with

$$J(\xi, k_y) = \int_0^{+\infty} dq\,\mathrm{FT}\{e^{ik_x\xi}\mathrm{Im}\{\hat{\tau}_l^x(k_x, k_y)\}\}\frac{1}{a}\sin(qa), \quad \text{and} \tag{C4}$$

$$Y(\xi, k_y) = \int_0^{+\infty} dq\,\mathrm{FT}\{ie^{ik_x\xi}\mathrm{Im}\{\hat{\tau}_l^y(k_x, k_y)\}\}\cos(qa), \tag{C5}$$

where FT denotes the Fourier transform along the k_x direction, namely,

$$\mathrm{FT}\{f(k_x)\}(q) = \frac{1}{\sqrt{2\pi}}\int_{-\infty}^{+\infty} dk_x\,e^{-iqk_x}f(k_x), \tag{C6}$$

and a is given by

$$a = \sqrt{\frac{f^2 + c_l^2 k_y^2}{U^2 - c_l^2}}. \tag{C7}$$

As already mentioned, this approach makes it possible to find the linear steady solution even in the case where the wind stress is not known analytically. Thus, in principle, the wind forcing could be given by observations.

APPENDIX D

Energy Propagation Speed

A sufficient condition to have an increase in the lateral energy propagation speed during the transfer of energy from a high-mode, near-inertial wave to a low-mode, double-inertial wave for an exponential stratification is here derived.

First of all, for lth-mode waves, the dispersion relation is

$$\omega_l = \sqrt{f^2 + c_l^2(k_x^2 + k_y^2)}, \tag{D1}$$

and the magnitude of the group speed as a function of frequency is

$$|\mathbf{c}_{gl}(\omega_l)| = c_l\sqrt{1 - \frac{f^2}{\omega_l^2}}. \tag{D2}$$

Therefore, at the Geisler frequency $\omega_l = \omega_{Gl}$ of Eq. (13) and at the double-inertial frequency $\omega_l = 2f$,

$$|\mathbf{c}_{gl}(\omega_{Gl})| = \frac{c_l^2}{U}, \quad \text{and} \tag{D3}$$

$$|\mathbf{c}_{gl}(2f)| = c_l\sqrt{\frac{3}{4}}. \tag{D4}$$

Considering now the ratio of the magnitude of the group speed of the mth mode at the near-inertial frequency ω_{Gm} to the magnitude of the group speed of the lth mode at the double-inertial frequency, one writes

$$Q_{m,l} = \frac{|\mathbf{c}_{gm}(\omega_{Gm})|}{|\mathbf{c}_{gl}(2f)|} = \frac{c_m^2/U}{c_l\sqrt{3/4}} = \frac{\overline{U}_{m,l}}{U}, \tag{D5}$$

with $\overline{U}_{m,l} = 2c_m^2/c_l\sqrt{3}$. If the condition $Q_{m,l} < 1$ is fulfilled, the transfer of energy from the mth-mode, near-inertial range to the lth-mode, double-inertial range results in an increase of the propagation velocity of the energy itself. The same condition can be written as $U > \overline{U}_{m,l}$. An analytical expression of $\overline{U}_{m,l}$ can be found in the case of exponential stratification of a deep ocean, that is, $N(z) = N_o e^{z/\lambda}$ with $z \in [-H, 0]$ and with $H/\lambda \gg 1$. In such a case, the eigenspeeds are given by the implicit condition

$$J_o(\lambda N_o/c_l) = 0, \tag{D6}$$

where $J_o(x)$ is the zeroth-order Bessel function of the first kind. Thus, if X_l denotes the lth zero of the function $J_o(x)$, the eigenspeeds are

$$c_l = \frac{\lambda N_o}{X_l}, \tag{D7}$$

and, in turn,

$$\overline{U}_{m,l} = \frac{2}{\sqrt{3}}\frac{X_l}{X_m^2}\lambda N_o. \tag{D8}$$

Since the zeros of the Bessel function J_o increases with l, one finds immediately that $\overline{U}_{m,l} \le \overline{U}_{2,1} \forall m > l$; thus, the condition on the ratio of the group speeds introduced above, $Q_{m,l} < 1$, becomes $U > \overline{U}_{2,1} \simeq \lambda N_o \times 10^{-1}$.

REFERENCES

Black, W. J., and T. D. Dickey, 2008: Observations and analyses of upper ocean responses to tropical storms and hurricanes in the vicinity of Bermuda. *J. Geophys. Res.*, **113**, C08009, doi:10.1029/2007JC004358.

Chang, S. W., and R. A. Anthes, 1978: Numerical simulations of the ocean's nonlinear, baroclinic response to translating hurricanes. *J. Phys. Oceanogr.*, **8**, 468–480, doi:10.1175/1520-0485(1978)008<0468:NSOTON>2.0.CO;2.

Danioux, E., and P. Klein, 2008: A resonance mechanism leading to wind-forced motions with a 2f frequency. *J. Phys. Oceanogr.*, **38**, 2322–2329, doi:10.1175/2008JPO3822.1.

D'Asaro, E. A., E. B. Sanford, P. P. Niiler, and E. J. Terrill, 2007: Cold wake of Hurricane Frances. *Geophys. Res. Lett.*, **34**, L15609, doi:10.1029/2007GL030160.

Debreu, L., P. Marchesiello, P. Penven, and G. Cambon, 2012: Two-way nesting in split-explicit ocean models: Algorithms, implementation and validation. *Ocean Modell.*, **49–50**, 1–21, doi:10.1016/j.ocemod.2012.03.003.

Eden, C., 2011: A closure for meso-scale eddy fluxes based on linear instability theory. *Ocean Modell.*, **39**, 362–369, doi:10.1016/j.ocemod.2011.05.009.

——, 2012: Implementing diffusivities from linear stability analysis in a three-dimensional general circulation ocean model. *Ocean Modell.*, **57–58**, 15–28, doi:10.1016/j.ocemod.2012.08.001.

Garrett, C., 2001: What is the "near-inertial" band and why is it different from the rest of the internal wave spectrum. *J. Phys. Oceanogr.*, **31**, 962–971, doi:10.1175/1520-0485(2001)031<0962:WITNIB>2.0.CO;2.

——, and W. Munk, 1972: Space-time scales of internal waves. *Geophys. Fluid Dyn.*, **3**, 225–264, doi:10.1080/03091927208236082.

——, and ——, 1975: Space-time scales of internal waves: A progress report. *J. Geophys. Res.*, **80**, 291–297, doi:10.1029/JC080i003p00291.

——, and ——, 1979: Internal waves in the ocean. *Annu. Rev. Fluid Mech.*, **11**, 339–369, doi:10.1146/annurev.fl.11.010179.002011.

Geisler, J. E., 1970: Linear theory of the response of a two layer ocean to a moving hurricane. *Geophys. Fluid Dyn.*, **1**, 249–272, doi:10.1080/03091927009365774.

Gerkema, T., L. R. M. Maas, and H. van Haren, 2013: A note on the role of mean flows in Doppler-shifted frequencies. *J. Phys. Oceanogr.*, **43**, 432–441, doi:10.1175/JPO-D-12-090.1.

Gill, A. E., 1982: *Atmosphere–Ocean Dynamics*. Academic Press, 662 pp.

——, 1984: On the behavior of internal waves in the wakes of storms. *J. Phys. Oceanogr.*, **14**, 1129–1151, doi:10.1175/1520-0485(1984)014<1129:OTBOIW>2.0.CO;2.

Greatbatch, R. J., 1984: On the response of the ocean to a moving storm: Parameters and scales. *J. Phys. Oceanogr.*, **14**, 59–78, doi:10.1175/1520-0485(1984)014<0059:OTROTO>2.0.CO;2.

Griesel, A., C. Eden, N. Koopmann, and E. Yulaeva, 2015: Comparing isopycnal eddy diffusivities in the Southern Ocean with predictions from linear theory. *Ocean Modell.*, **94**, 33–45, doi:10.1016/j.ocemod.2015.08.001.

Heywood, K. J., A. C. Naveira Garabato, and D. P. Stevens, 2002: High mixing rates in the abyssal Southern Ocean. *Nature*, **415**, 1011–1014, doi:10.1038/4151011a.

Hibiya, T., Y. Niwa, K. Nakajima, and N. Suginohara, 1996: Direct numerical simulation of the roll-off range of internal wave shear spectra in the ocean. *J. Geophys. Res.*, **101**, 14 123–14 129, doi:10.1029/96JC01001.

Jackett, D. R., and T. McDougall, 1995: Minimal adjustment of hydrographic profiles to achieve static stability. *J. Atmos. Oceanic Technol.*, **12**, 381–389, doi:10.1175/1520-0426(1995)012<0381:MAOHPT>2.0.CO;2.

Jansen, M., and R. Ferrari, 2009: Impact of the latitudinal distribution of tropical cyclones on ocean heat transport. *Geophys. Res. Lett.*, **36**, L06604, doi:10.1029/2008GL036796.

——, ——, and T. A. Mooring, 2010: Seasonal versus permanent thermocline warming by tropical cyclones. *Geophys. Res. Lett.*, **37**, L03602, doi:10.1029/2009GL041808.

Korty, R. L., K. A. Emanuel, and J. R. Scott, 2008: Tropical cyclone-induced upper-ocean mixing and climate: Application to equable climates. *J. Climate*, **21**, 638–654, doi:10.1175/2007JCLI1659.1.

Kroll, J., 1975: Propagation of wind-generated inertial oscillations from surface into deep ocean. *J. Mar. Res.*, **33**, 15–51.

Kundu, K. P., and R. E. Thomson, 1985: Inertial oscillations due to a moving front. *J. Phys. Oceanogr.*, **15**, 1076–1084, doi:10.1175/1520-0485(1985)015<1076:IODTAM>2.0.CO;2.

Large, W. G., J. C. McWilliams, and S. C. Doney, 1994: Oceanic vertical mixing: A review and a model with a nonlocal

boundary layer parametrization. *Rev. Geophys.*, **32**, 363–403, doi:10.1029/94RG01872.

Ledwell, J. R., A. J. Watson, and C. S. Law, 1993: Evidence for slow mixing across the pycnocline from an open-ocean tracer-release experiment. *Nature*, **364**, 701–703, doi:10.1038/364701a0.

——, ——, and ——, 1998: Mixing of a tracer in the pycnocline. *J. Geophys. Res.*, **103**, 21 499–21 529, doi:10.1029/98JC01738.

——, E. T. Montgomery, K. L. Polzin, L. C. St. Laurent, R. W. Schmitt, and J. M. Toole, 2000: Evidence for enhanced mixing over rough topography in the abyssal ocean. *Nature*, **403**, 179–182, doi:10.1038/35003164.

Lighthill, M. J., 1978: *Waves in Fluids*. Cambridge University Press, 504 pp.

McComas, C. H., and F. P. Bretherton, 1977: Resonant interaction of oceanic internal waves. *J. Geophys. Res.*, **82**, 1397–1412, doi:10.1029/JC082i009p01397.

——, and P. Müller, 1981: The dynamic balance of internal waves. *J. Phys. Oceanogr.*, **11**, 970–986, doi:10.1175/1520-0485(1981)011<0970:TDBOIW>2.0.CO;2.

Mei, W., C. Pasquero, and F. Primeau, 2012: The effect of translation speed upon the intensity of tropical cyclones over the tropical ocean. *Geophys. Res. Lett.*, **39**, L07801, doi:10.1029/2011GL050765.

Müller, P., G. Holloway, F. Henyey, and N. Pomphrey, 1986: Nonlinear interactions among internal gravity waves. *Rev. Geophys.*, **24**, 493–536, doi:10.1029/RG024i003p00493.

Munk, W., 1981: Internal wave and small-scale processes. *Evolution of Physical Oceanography*, B. A. Warren and C. Wunsch, Eds., MIT Press, 264–291.

——, and C. Wunsch, 1998: Abyssal recipes II: Energetics of tidal and wind mixing. *Deep-Sea Res.*, **45**, 1977–2010, doi:10.1016/S0967-0637(98)00070-3.

Nilsson, J., 1995: Energy flux from traveling hurricanes to the oceanic internal wave field. *J. Phys. Oceanogr.*, **25**, 558–573, doi:10.1175/1520-0485(1995)025<0558:EFFTHT>2.0.CO;2.

Niwa, Y., and T. Hibiya, 1997: Nonlinear processes of energy transfer from traveling hurricanes to the deep ocean internal wave field. *J. Geophys. Res.*, **102**, 12 469–12 477, doi:10.1029/97JC00588.

Olbers, D., 1974: *On the Energy Balance of Small-Scale Internal Waves in the Deep-Sea*. Hamburg Geophysikalische Einzelschriften, 91 pp.

——, 1976: Nonlinear energy transfer and the energy balance of the internal wave field in the deep ocean. *J. Fluid Mech.*, **74**, 375–399, doi:10.1017/S0022112076001857.

——, and C. Eden, 2013: A global model for the diapycnal diffusivity induced by internal gravity waves. *J. Phys. Oceanogr.*, **43**, 1759–1779, doi:10.1175/JPO-D-12-0207.1.

——, J. Willebrand, and C. Eden, 2012: *Ocean Dynamics*. 1st ed. Springer, 708 pp.

Pasquero, C., and K. Emanuel, 2008: Tropical cyclones and transient upper-ocean warming. *J. Climate*, **21**, 149–162, doi:10.1175/2007JCLI1550.1.

Penven, P., L. Debreu, P. Marchesiello, and J. C. McWilliams, 2006: Evaluation and application of the ROMS 1-way embedding procedure to the central California Upwelling System. *Ocean Modell.*, **12**, 157–187, doi:10.1016/j.ocemod.2005.05.002.

Phillips, O. M., 1966: *The Dynamics of the Upper Ocean*. 1st ed. Cambridge University Press, 261 pp.

Pickard, G. L., and W. J. Emery, 1990: *Descriptive Physical Oceanography*. 5th ed. Pergamon Press, 321 pp.

Pollard, R. T., 1970: On the generation by winds of inertial waves in the ocean. *Deep-Sea Res. Oceanogr. Abstr.*, **17**, 795–812, doi:10.1016/0011-7471(70)90042-2.

Polzin, K. L., J. M. Toole, J. R. Ledwell, and R. W. Schmitt, 1997: Spatial variability of turbulent mixing in the abyssal ocean. *Science*, **276**, 93–96, doi:10.1126/science.276.5309.93.

Pomphrey, N., J. D. Meiss, and K. M. Watson, 1980: Description of nonlinear internal wave interactions using Langevin methods. *J. Geophys. Res.*, **85**, 1085–1094, doi:10.1029/JC085iC02p01085.

Price, J. F., 1981: Upper ocean response to a hurricane. *J. Phys. Oceanogr.*, **11**, 153–175, doi:10.1175/1520-0485(1981)011<0153:UORTAH>2.0.CO;2.

——, 1983: Internal wave wake of a moving storm. Part I: Scales, energy budget and observations. *J. Phys. Oceanogr.*, **13**, 949–965, doi:10.1175/1520-0485(1983)013<0949:IWWOAM>2.0.CO;2.

Ripa, P., 1981: On the theory of nonlinear wave-wave interactions among geophysical waves. *J. Fluid Mech.*, **103**, 87–115, doi:10.1017/S0022112081001250.

Rubenstein, D., 1994: A spectral model of wind-forced internal waves. *J. Phys. Oceanogr.*, **24**, 819–831, doi:10.1175/1520-0485(1994)024<0819:ASMOWF>2.0.CO;2.

Samson, G., H. Giordani, G. Caniaux, and F. Roux, 2009: Numerical investigation of an oceanic resonant regime induced by hurricane winds. *Ocean Dyn.*, **59**, 565–586, doi:10.1007/s10236-009-0203-8.

Sanford, T. B., J. F. Price, J. B. Girton, and D. C. Webb, 2007: Highly resolved observations and simulations of the ocean response to a hurricane. *Geophys. Res. Lett.*, **34**, L13604, doi:10.1029/2007GL029679.

Shay, L. K., R. L. Elseberry, and P. G. Black, 1989: Vertical structure of the ocean current response to a hurricane. *J. Phys. Oceanogr.*, **19**, 649–669, doi:10.1175/1520-0485(1989)019<0649:VSOTOC>2.0.CO;2.

Shchepetkin, A. F., and J. C. McWilliams, 2003: A method for computing horizontal pressure-gradient force in an oceanic model with a nonaligned vertical coordinate. *J. Geophys. Res.*, **108**, 3090, doi:10.1029/2001JC001047.

Sjöberg, B., and A. Stigebrandt, 1992: Computations of the geographical distribution of the energy flux to mixing processes via internal tides and the associated vertical circulation in the ocean. *Deep-Sea Res.*, **39**, 269–291, doi:10.1016/0198-0149(92)90109-7.

Sriver, R. L., and M. Huber, 2007: Observational evidence for an ocean heat pump induced by tropical cyclones. *Nature*, **447**, 577–580, doi:10.1038/nature05785.

Staquet, C., and J. Sommeria, 2002: Internal gravity waves: From instabilities to turbulence. *Annu. Rev. Fluid Mech.*, **34**, 559–593, doi:10.1146/annurev.fluid.34.090601.130953.

Thorpe, S. A., 2005: *The Turbulent Ocean*. 1st ed. Cambridge University Press, 439 pp.

Wagner, G. L., and W. R. Young, 2016: A three-component model for the coupled evolution of near-inertial waves, quasi-geostrophic flow and the near-inertial second harmonic. *J. Fluid Mech.*, **802**, 806–837, doi:10.1017/jfm.2016.487.

Waterhouse, A. F., and Coauthors, 2014: Global patterns of diapycnal mixing from measurements of the turbulent dissipation rate. *J. Phys. Oceanogr.*, **44**, 1854–1872, doi:10.1175/JPO-D-13-0104.1.

Whalen, C. B., L. D. Talley, and J. A. Mackinnon, 2012: Spatial and temporal variability of global ocean mixing inferred from Argo profiles. *Geophys. Res. Lett.*, **39**, L18612, doi:10.1029/2012GL053196.

Xie, X., Q. Liu, X. Shang, G. Chen, and D. Wang, 2016: Poleward propagation of parametric subharmonic instability-induced inertial waves. *J. Geophys. Res. Oceans*, **121**, 1881–1895, doi:10.1002/2015JC011194.

Zedler, S. E., 2009: Simulations of the ocean response to a hurricane: Nonlinear processes. *J. Phys. Oceanogr.*, **39**, 2618–2634, doi:10.1175/2009JPO4062.1.